Chapter 3
Autocalibration of MEMS Accelerometers

Iuri Frosio, Federico Pedersini, and N. Alberto Borghese

Abstract In this chapter, we analyze the critical aspects of the widely diffused calibration and autocalibration procedures for MEMS accelerometers. After providing a review of the main applications of this kind of sensors, we introduce the different sensor models proposed in literature, highlighting the role of the axis misalignments in the sensor sensitivity matrix. We derive a principled noise model and discuss how noise affects the norm of the measured acceleration vector. Since autocalibration procedures are based on the assumption that the norm of the measured acceleration vector, in static condition, equals the gravity acceleration, we introduce the international gravity formula, which provides a reliable estimate of the gravity acceleration as a function of the local latitude and altitude. We derive then the autocalibration procedure in the context of maximum likelihood estimate and we provide examples of calibrations. For each calibrated sensor, we also illustrate how to derive the accuracy on the estimated parameters through the covariance analysis and how to compute the angles between the sensing axes of the sensor. In the conclusion, we summarize the main aspects involved in the autocalibration of MEMS accelerometers.

3.1 Introduction

The advent of microelectromechanical system (MEMS) technology has allowed miniaturized, high performance and cheap accelerometers to be built using a variety of different approaches [1–3]. These sensors were initially used to detect sudden, critical events like in airbag control [4], but nowadays applications cover a wide range of fields, briefly described in the following. A common factor for many applications is that an accurate measurement of the local acceleration is needed, but MEMS sensors

I. Frosio (✉) • F. Pedersini • N. Alberto Borghese
Computer Science Department, University of Milan, Via Comelico 39/41, Milano 20135, Italy
e-mail: iuri.frosio@unimi.it; federico.pedersini@unimi.it; alberto.borghese@unimi.it

are only imprecisely (or not at all) calibrated after production; therefore, a practical and precise sensor calibration procedure is necessary to get satisfying accuracy.

MEMS accelerometers are used, in static or quasi-static conditions, as tilt sensors [5] and to reconstruct the movements of human body segments [6–10]. A surveillance application is for instance described in [9], where the analysis of the signal measured by an accelerometer on the trunk of the subject permits to classify human activities and posture transitions with an accuracy higher than 90 %. In [6], a wearable device containing several accelerometers and gyroscopes is used to track and analyze the movements of body segments; the sensor calibration permits to limit the effect of the drift: the experimental results reported in the paper revealed positioning errors smaller than 6 mm and angular errors smaller than 0.2° during the acquisition of a typical sit-to-stand movement; such accuracy is comparable to that of a traditional motion capture system, which is however more costly and cumbersome. An algorithm for the on-line, automatic recalibration of the accelerometer is proposed in [10], where another medical application of the accelerometers is described; calibration is in this case necessary to guarantee that the accuracy of the sensor remains constant over the time, as its output changes significantly, for instance, with respect to the external temperature or other physical quantities.

MEMS accelerometers are also widely employed in Inertial Measurements Units (IMUs), together with gyroscopes and magnetometers, to track the motion of a pedestrian [11], terrestrial [12–14] or even aerial vehicles [15]. In [11], the authors suggest using a wearable IMU comprising accelerometers and magnetometers to track a pedestrian; an accurate calibration procedure of the IMU sensors is essential for this application; in particular, the misalignment of the sensor axes has to be explicitly taken into account to guarantee a satisfying accuracy of the tracking procedure. In [13], an IMU is used to track the position of a car when the GPS signal is lost; if the sensor is not calibrated before its use, a position error larger than 2.5 km can be accumulated during a 60 s loss of the GPS signal; a calibrated sensor limits the position drift to less than 400 m. The same authors describe in [14] an integrated IMU/GPS system, where the drifts of the offsets and sensitivities of the sensor with respect to the temperature are taken into account by a proper thermal variation model. A similar IMU system is considered in [15] to track the position and orientation of a small helicopter; also in this case, a model of the accelerometers including non-orthogonal axes and the corresponding calibration procedure are described.

In a slightly different scenario, MEMS accelerometers are also used to integrate traditional tracking systems based on vision technology [16]. In fact, vision based tracking systems are generally capable of tracking objects, without introducing drifts, at low frequencies (a camera acquires typically images at a rate of 60 frames per second); accelerometer based procedures generate data at a significantly higher frequency; they are used in [16] to track the movement of an object between the acquisition of two consequent frames, therefore increasing the tracking frequency to hundreds of Hertz.

Other quasi-static applications of the accelerometers requiring an accurate measurements of the local acceleration vectors include, but are not limited to, handwriting recording [17], real-time character recognition [18], quantification of

the physical activity of a subject [19], analysis of sport equipment during movements [20], and so on.

A common factor to all these applications is that the sensors are used in quasi-static condition; therefore, they measure an acceleration which is supposed to be slowly varying with time. Modeling the frequency response of the sensor is generally not necessary for this kind of applications; however, an accurate calibration is needed to avoid drifts that may turn the measured acceleration into an untrustworthy position measurement in a short time.

Other applications of the accelerometers include a dynamic usage, for instance controlling damages of mechanical structures [21, 22] or seismography [23]. In this case, the output of the accelerometer has to be characterized over the entire frequency domains and specific calibration procedures have been proposed to this aim: this goes beyond the scope of this chapter.

The chapter is organized as follows: after this brief introduction, where different applications of the MEMS accelerometers have been reviewed, the sensor models adopted by various authors in literature are briefly described. In the same section, it is also illustrated the matrix decomposition procedure that allows passing from a symmetric to a left triangular sensitivity matrix. The next section introduces a novel, principled noise model for MEMS accelerometers and clearly illustrates the effect of the noise on the measurements of small accelerations. Afterwards, the importance of correcting for local gravity variations is highlighted. The autocalibration procedure is described in the subsequent section, where a novel derivation of the procedure in the context of maximum likelihood estimate is derived. The autocalibration results obtained on different accelerometers are illustrated and discussed, and a brief review of the main concepts closes the chapter.

3.2 Sensor Models

Different sensor models have been proposed in literature, to describe the relation between the acceleration applied to the sensor and its output. These models differ for their complexity (i.e., number of model parameters); generally speaking, the more complex is the model, the more accurate is the description of the physics of the sensor; on the other hand, complex models also require complex (i.e., costly, time-consuming, or requiring specific hardware) calibration procedures, and they suffer the risk of overfitting. Therefore, depending on the specific application, the best compromise between the model accuracy and its complexity has to be found.

For instance, in [9] it is assumed that the three axes of the accelerometer produce the same output voltage when they are solicited by the same force; such simple model is described by the following equation:

$$\mathbf{v} = V_{CC} \left(\begin{bmatrix} s & 0 & 0 \\ 0 & s & 0 \\ 0 & 0 & s \end{bmatrix} \mathbf{a}' + \begin{bmatrix} o \\ o \\ o \end{bmatrix} \right), \tag{3.1}$$

where $\mathbf{v}$ is a 3×1 vector representing the three voltages output by the sensor, $\mathbf{a}'$ is the acceleration vector in the reference system of the sensor,[1] whereas s and o represent the sensitivity and offset of each channel. The parameter V_{CC} represents the power supply voltage, and it is introduced here to take into account that the major part of the MEMS accelerometers is ratiometric [4]. Notice that, although this model is quite simplistic, it is sufficient to recognize with high accuracy the posture of a human being [9]; however, a more realistic model is needed for applications requiring a higher accuracy.

In [23] and [10], a six-parameter model is considered, representing a sensor with different offset and sensitivity for each channel. This is described by:

$$\mathbf{v} = V_{CC} \left(\begin{bmatrix} s_X & 0 & 0 \\ 0 & s_Y & 0 \\ 0 & 0 & s_Z \end{bmatrix} \mathbf{a}' + \begin{bmatrix} o_X \\ o_Y \\ o_Z \end{bmatrix} \right), \tag{3.2}$$

where s_k and o_k represent respectively the sensitivity and the offset of the kth sensor channel. Equation (3.2) can take into account, for instance, the different weight of the proof masses used by the three channels of the accelerometer, or the different stiffness of their supporting arms, introduced during the fabrication of the sensor.

This model, however, cannot give account of the misalignments of the three axes of the sensor. Small misalignments are in fact introduced by a not perfectly controlled fabrication process; even more important, large deviations from set of three orthogonal axes can be measured when a triaxial accelerometer is obtained putting together mono or biaxial accelerometers, like for instance in [5].

The sensor model which includes the axes misalignment requires nine parameters, and it is the most widely adopted for the description of the accelerometers [4, 11, 13, 15, 24] and, more in general, of any triaxial sensor [25]. To derive the model, we have to consider that the vector $\mathbf{a}'$ in (3.1) and (3.2) represents the three projections of the local acceleration vector, $\mathbf{a}$, onto the three non orthogonal sensing axes of the sensor. To put in relation $\mathbf{a}$ and $\mathbf{a}'$, we have to consider a set of rotation matrices that define the relationship of the misaligned axes, $\{\mathbf{X}', \mathbf{Y}', \mathbf{Z}'\}$ to those of the perfectly orthogonal reference system, $\{\mathbf{X}, \mathbf{Y}, \mathbf{Z}\}$ (Fig. 3.1). To this aim let us first assume, without loss of generality, that axes $\mathbf{X}$ and $\mathbf{X}'$ are coincident and that, in the sensor reference system, they are both equal to $[1\ 0\ 0]^T$. The $\mathbf{Y}'$ axis is obtained rotating $\mathbf{Y}$ around the Z axis by an angle α_{ZY} (see Fig. 3.1); therefore, its coordinates, in the orthogonal reference system defined by $\{\mathbf{X}, \mathbf{Y}, \mathbf{Z}\}$, are given by:

$$\mathbf{Y}' = \begin{bmatrix} c(\alpha_{ZY}) & -s(\alpha_{ZY}) & 0 \\ s(\alpha_{ZY}) & c(\alpha_{ZY}) & 0 \\ 0 & 0 & 1 \end{bmatrix} \begin{bmatrix} 0 \\ 1 \\ 0 \end{bmatrix} = \begin{bmatrix} -s(\alpha_{ZY}) \\ c(\alpha_{ZY}) \\ 0 \end{bmatrix}, \tag{3.3}$$

---

[1] Each component of $\mathbf{a}'$ represents the projection of the local acceleration vector onto one of the sensing axes of the sensor; these are not necessarily orthogonal to each other.

Fig. 3.1 The geometrical model adopted to describe the misalignments of the sensor axes
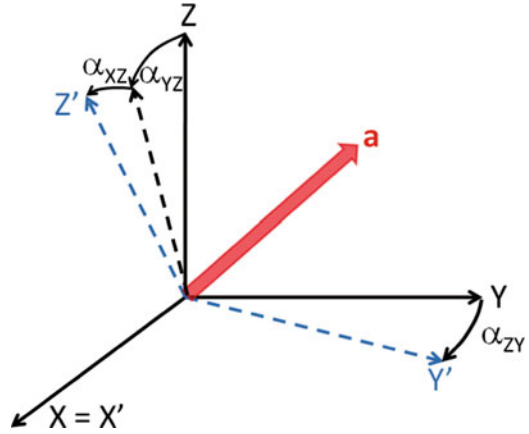
where $c(t)$ and $s(t)$ indicate respectively the $\cos(t)$ and $\sin(t)$ functions. The $\mathbf{Z}'$ axis is obtained rotating $\mathbf{Z}$ around the Y axis, by an angle α_{YZ}, and then around the X axis, by an angle α_{XZ}. Its coordinates are therefore given by:

$$
\mathbf{Z}' = \begin{bmatrix} 1 & 0 & 0 \\ 0 & c(\alpha_{XZ}) & -s(\alpha_{XZ}) \\ 0 & s(\alpha_{XZ}) & c(\alpha_{XZ}) \end{bmatrix} \begin{bmatrix} c(\alpha_{YZ}) & 0 & s(\alpha_{YZ}) \\ 0 & 1 & 0 \\ -s(\alpha_{YZ}) & 0 & c(\alpha_{YZ}) \end{bmatrix} \begin{bmatrix} 0 \\ 0 \\ 1 \end{bmatrix}
$$

$$
= \begin{bmatrix} -s(\alpha_{YZ}) \\ -s(\alpha_{XZ})c(\alpha_{YZ}) \\ c(\alpha_{XZ})c(\alpha_{YZ}) \end{bmatrix}. \tag{3.4}
$$

The components of the vector $\mathbf{a}'$ are obtained projecting $\mathbf{a}$ onto the three axes X', Y', Z'; such process is described by:

$$
\mathbf{a}' = \begin{bmatrix} 1 & 0 & 0 \\ -s(\alpha_{ZY}) & c(\alpha_{ZY}) & 0 \\ -s(\alpha_{YZ}) & -s(\alpha_{XZ})c(\alpha_{YZ}) & c(\alpha_{XZ})c(\alpha_{YZ}) \end{bmatrix} \mathbf{a}. \tag{3.5}
$$

By substituting (3.5) into (3.2), we finally obtain the model of the accelerometer including three sensitivities, three offsets, and three angles (associated to axes misalignments), which is given by:

$$
\mathbf{v} = V_{CC} \left(\begin{bmatrix} s_X & 0 & 0 \\ -s_Y s(\alpha_{ZY}) & s_Y c(\alpha_{ZY}) & 0 \\ -s_Z s(\alpha_{YZ}) & -s_Z s(\alpha_{XZ})c(\alpha_{YZ}) & s_Z c(\alpha_{XZ})c(\alpha_{YZ}) \end{bmatrix} \mathbf{a} + \begin{bmatrix} o_X \\ o_Y \\ o_Z \end{bmatrix} \right). \tag{3.6}
$$

In practice, this model includes a 3×3 lower triangular matrix, $\mathbf{S}$, to represent the sensitivity of the sensor and the axes misalignments, and a 3×1 vector, $\mathbf{o}$, to represent the offset on each channel:

$$\mathbf{v} = V_{CC}(\mathbf{Sa} + \mathbf{o}). \tag{3.7}$$

It is adopted by most authors [11, 13, 15, 24, 25]. More generally, any 3×3 matrix with six free parameters could be adopted to describe the sensor sensitivity and the axes misalignment. For instance, in [4], we assumed the sensitivity matrix to be a 3×3 symmetric matrix; such assumption simply corresponds to a rotation of the sensor reference system assumed here to describe the local acceleration vector, $\mathbf{a}$. Such rotation can be decomposed into a sequence of three rotations occurring around the three axes of the reference system, and it is described by a proper 3×3 matrix, $\mathbf{R}$. The relation between the lower triangular sensitivity matrix $\mathbf{S}$, in (3.7), and the symmetric sensitivity matrix $\mathbf{S}'$, adopted in [4], is therefore: $\mathbf{S} = \mathbf{RS}'$; the matrix $\mathbf{R}$ can be obtained from $\mathbf{S}'$ extracting the sequence of three Givens rotations that transform $\mathbf{S}'$ into $\mathbf{S}$ [26].

An example of such matrix decomposition is illustrated in the following. In particular, to illustrate how the decomposition works, let us consider the following sensitivity matrix:

$$\mathbf{S}' = \begin{bmatrix} 0.0188 & -0.0004 & -0.0006 \\ -0.0004 & 0.0185 & -0.0002 \\ -0.0006 & -0.0002 & 0.0207 \end{bmatrix}. \tag{3.8}$$

This matrix was computed for a typical triaxial MEMS accelerometer (the LIS3L02AL by ST Microelectronics [27]) with the autocalibration procedure described in this chapter and, more specifically, this is the matrix associated to the sensor #3 in Tables 3.6, 3.7 and 3.8.

The first two Givens rotations have to delete the first and second elements of the third column of $\mathbf{S}'$. Notice that the three columns of $\mathbf{S}'$ can be interpreted as a set of three non orthogonal axes. The first two terms of the third column can then be zeroed by a proper rotation around the X axis, followed by a proper rotation around the Y axis. In particular, from the explicit form of two rotation matrices around the X and Y axes applied to $\mathbf{S}'$, we obtain:

$$\mathbf{S^{XY}} = \mathbf{R_Y R_X S}' = \begin{bmatrix} \cos(R_Y) & 0 & -\sin(R_Y) \\ 0 & 1 & 0 \\ \sin(R_Y) & 0 & \cos(R_Y) \end{bmatrix} \begin{bmatrix} 1 & 0 & 0 \\ 0 & \cos(R_X) & \sin(R_X) \\ 0 & -\sin(R_X) & \cos(R_X) \end{bmatrix} \mathbf{S}',$$

$$S_{YZ}^{XY} = \cos(R_X)S_{YZ}' + \sin(R_X)S_{ZZ}' = 0 \Rightarrow R_X = -\tan^{-1}\left(\frac{S_{YZ}'}{S_{ZZ}'}\right),$$

$$S_{XZ}^{XY} = \cos(R_Y)S_{XZ}' - \sin(R_Y)\cos(R_X)S_{ZZ}' + \sin(R_Y)\sin(R_X)S_{YZ}' = 0,$$

$$\Rightarrow R_Y = \tan^{-1}\left[\frac{-S_{XZ}'}{-\cos(R_X)S_{ZZ}' + \sin(R_X)S_{YZ}'}\right], \tag{3.9}$$

where $\mathbf{S^{XY}}$ is the sensitivity matrix $\mathbf{S'}$ rotated by $\mathbf{R_X}$ and $\mathbf{R_Y}$; R_X and R_Y are the angles of rotation around the X and Y axes; S^{XY}_{YZ} and S^{XY}_{XZ} are respectively the element on the second row, third column and on the first row, third column of $\mathbf{S^{XY}}$; S'_{ij} represents the elements in position ij of $\mathbf{S'}$. For the matrix $\mathbf{S'}$ in (3.8), we obtain $R_X = 0.5903°$ and $R_Y = -1.5431°$ and the resulting matrix $\mathbf{S^{XY}}$ is:

$$\mathbf{S^{XY}} = \mathbf{R_Y R_X S} = \begin{bmatrix} 0.0188 & -0.0004 & 0 \\ -0.0004 & 0.0185 & 0 \\ -0.0011 & -0.0004 & 0.0207 \end{bmatrix}. \tag{3.10}$$

To get a lower triangular matrix from (3.10), a further rotation matrix representing a rotation around the Z axis has to be applied to $\mathbf{S^{XY}}$. Notice, in fact, that the third column of $\mathbf{S^{XY}}$ is parallel to the Z axis, and it is therefore not affected by a rotation around it; as a consequence, after the application of such rotation, the first and second element of the third column of $\mathbf{S^{XY}}$ remain zeros. The third Givens rotation is therefore obtained from the explicit form of the matrix $\mathbf{R_Z}$, representing a rotation of an angle R_Z around the Z axis, applied to $\mathbf{S^{XY}}$; this gives:

$$\mathbf{S} = \mathbf{R_Z S^{XY}} = \begin{bmatrix} \cos(R_Z) & \sin(R_Z) & 0 \\ \sin(R_Z) & \cos(R_Z) & 0 \\ 0 & 0 & 1 \end{bmatrix} \mathbf{S^{XY}},$$

$$S_{XY} = \cos(R_Z)S^{XY}_{XY} + \sin(R_Z)S^{XY}_{YY} = 0 \Rightarrow R_Z = -\tan^{-1}\left(\frac{S^{XY}_{XY}}{S^{XY}_{YY}}\right). \tag{3.11}$$

The rotation angle around the Z axis for $\mathbf{S}$ in (3.11) results to be $R_Z = 1.3683°$; after application of $\mathbf{R_Z}$ to $\mathbf{S^{XY}}$, we obtain the decomposition of the symmetric matrix $\mathbf{S'}$ into a rotation matrix $\mathbf{R}$ and a triangular matrix $\mathbf{S}$ as:

$$\mathbf{S} = \mathbf{R_Z R_Y R_X S'} = \mathbf{R S'},$$

$$\mathbf{R} = \begin{bmatrix} 0.9994 & 0.0236 & 0.0272 \\ -0.0239 & 0.9997 & 0.0097 \\ -0.0269 & -0.0103 & 0.9996 \end{bmatrix},$$

$$\mathbf{S} = \begin{bmatrix} 0.0188 & 0 & 0 \\ -0.0009 & 0.0185 & 0 \\ -0.0011 & -0.0004 & 0.0207 \end{bmatrix}. \tag{3.12}$$

The lower triangular matrix $\mathbf{S}$ in (3.12) represents therefore the sensor sensitivity matrix as in (3.6); the three rows represent three vectors whose magnitude is equal to the sensitivity of the associated channel; in particular, we obtain in this case: $s_X = 0.0188$ V/(m/s^2), $s_Y = 0.0186$ V/(m/s^2), $s_Z = 0.0208$ V/(m/s^2). Moreover, these vectors are aligned with the axes of the sensor; we can therefore estimate

angle between the axes. For instance, the angle between the X and Y axis for the matrix $\mathbf{S}$ in (3.12) is obtained as:

$$XY = \cos^{-1}\left(\frac{[0.0188 \quad 0 \quad 0][-0.0009 \quad 0.0185 \quad 0]^T}{\sqrt{0.0188^2 + 0^2 + 0^2}\sqrt{(-0.0009)^2 + 0.0185^2 + 0^2}}\right)$$
$$= 92.737°. \tag{3.13}$$

The angles between the other axes are obtained in a similar manner.

To summarize, (3.7) represents the commonly adopted model to describe the relation between the acceleration vector in the sensor reference system, $\mathbf{a}$, and the voltage output of the sensor, $\mathbf{v}$. The 3×3 sensitivity matrix, $\mathbf{S}$, contains six free parameters that have to be estimated during the calibration procedure. $\mathbf{S}$ is generally assumed to be left triangular or symmetric; decomposition of a symmetric matrix through a set of three Givens rotations allows computing the corresponding left triangular matrix and the rotation matrix which transform one into the other. From the triangular matrix, the angles between the sensor axes can finally be derived.

Many experimental results, reported for instance in [4, 16], suggest that models of quasi static accelerometers with number of parameters higher than nine are generally not justifiable, as the additional parameters cannot be reliably estimated by the existing calibration procedures. In [4], we considered a sensitivity matrix with 12 free parameters; the experimental results demonstrate that such model does not provide better results than the nine parameters model, and the additional parameters are estimated with low accuracy. In [16], a model including the sensor nonlinearity is analyzed, but the authors conclude that the parameters associated to the nonlinearity cannot be reliably estimated and the linear model performs better.

Other sensor models, tailored to specific applications, may include the dependency of $\mathbf{S}$ and $\mathbf{o}$ from the temperature or other physical parameters [14]. However, a sensor model including these parameters require a costly and time consuming calibration procedure, where data are acquired at a set of different, controlled temperatures. When possible, it is preferable to use a nine model parameters and calibrate the sensor on the field and to track in real time the changes of $\mathbf{o}$ and $\mathbf{S}$, as done, for instance, in [9].

Finally, we notice that also sensor models representing the frequency response of the sensor have been proposed for applications like seismography [23] or mechanical testing [21, 22]. In this case, the output of the accelerometer has to be characterized over the entire frequency domain and specific calibration procedures have been proposed to this aim. As already noted in the former chapter, this goes beyond the scope of this chapter; the sensor model and the autocalibration procedure described here could however be applied also in these cases, to accurately characterize the response of the sensor at zero frequency.

3.3 Noise Model

Although the major part of the authors spent a lot of time to describe the physical models of the sensor, only a few of them (see for instance [25]) spent some words about the inclusion of the noise into the sensor model; actually this constitutes a critical point for many of the calibration procedures in the literature, as the cost function associated to the calibration procedure should be strictly related to the characteristics of the noise present on the calibration data. Here we introduce a novel, reasonable noise model and we analyze how this affects the measured acceleration vector and the calibration procedures.

In the following, we assume that additive, white noise with zero mean and Gaussian distribution is present on each output channel of the accelerometer. In particular, let us indicate with $G_M(\sigma^2)$ a column vector with M components where each component is a Gaussian random variable with zero mean and variance σ^2 and let us define the noise vector $\mathbf{n} \sim G_3(\sigma^2)$. The noisy sensor output is therefore defined as:

$$\mathbf{v_n} = V_{CC}(\mathbf{Sa} + \mathbf{o}) + \mathbf{n}. \tag{3.14}$$

Inverting (3.14), we obtain the estimated acceleration vector, $\mathbf{a_n}$, from the output of the accelerometer, which is:

$$\mathbf{a_n} = \mathbf{S}^{-1}\left(\frac{\mathbf{v_n}}{V_{CC}} - \mathbf{o}\right) = \mathbf{S}^{-1}\left(\frac{\mathbf{v}}{V_{CC}} - \mathbf{o}\right) - \mathbf{S}^{-1}\frac{\mathbf{n}}{V_{CC}}. \tag{3.15}$$

The first term in (3.15), $\mathbf{S}^{-1}(\mathbf{v}/V_{CC} - \mathbf{o})$, represents the real acceleration vector, whereas the term $-\mathbf{S}^{-1}\mathbf{n}/V_{CC}$ is the noise contribution. Here we will analyze the effect of the noise term on the length of $\mathbf{a_n}$ and we will show how this can affect a sensor calibration procedure. To this aim, let us consider the expected value of the squared norm of $\mathbf{a_n}$, which is given by:

$$
\begin{aligned}
E[\mathbf{a_n}^T\mathbf{a_n}] &= E\left[\left\{\mathbf{S}^{-1}\left(\frac{\mathbf{v_n}}{V_{CC}} - \mathbf{o}\right)\right\}^T \mathbf{S}^{-1}\left(\frac{\mathbf{v_n}}{V_{CC}} - \mathbf{o}\right)\right], \\
&= E\left[\left\{\mathbf{S}^{-1}\left(\frac{\mathbf{v}}{V_{CC}} - \mathbf{o}\right) - \mathbf{S}^{-1}\frac{\mathbf{n}}{V_{CC}}\right\}^T \left\{\mathbf{S}^{-1}\left(\frac{\mathbf{v}}{V_{CC}} - \mathbf{o}\right) - \mathbf{S}^{-1}\frac{\mathbf{n}}{V_{CC}}\right\}\right], \\
&= \left(\frac{\mathbf{v}}{V_{CC}} - \mathbf{o}\right)^T \mathbf{S}^{-T}\mathbf{S}^{-1}\left(\frac{\mathbf{v}}{V_{CC}} - \mathbf{o}\right) - 2E\left[\left(\mathbf{S}^{-1}\frac{\mathbf{n}}{V_{CC}}\right)^T\right]\mathbf{S}^{-1}\left(\frac{\mathbf{v}}{V_{CC}} - \mathbf{o}\right) \\
&\quad + \frac{E\left[(\mathbf{S}^{-1}\mathbf{n})^T\mathbf{S}^{-1}\mathbf{n}\right]}{V_{CC}^2},
\end{aligned}
\tag{3.16}
$$

where $E[x]$ indicates the expected value of x. The first term in (3.16) is associated to the true acceleration vector, whereas the second and third terms are noise contributes.

The second term is zero as the expected value of $\mathbf{n}$ is zero for each component; in fact:

$$E\left[\left(\mathbf{S}^{-1}\frac{\mathbf{n}}{V_{CC}}\right)^{\mathrm{T}}\right] = E\left[\mathbf{n}^{\mathrm{T}}\right]\frac{\mathbf{S}^{-\mathrm{T}}}{V_{CC}} = 0. \tag{3.17}$$

To characterize the effect of the third term in (3.16), we approximate $\mathbf{S}$ with a diagonal matrix, with diagonal elements equal to $s*$; also $\mathbf{S}^{-1}$ is in this case diagonal, with diagonal elements equal to $1/s*$. Such approximation corresponds to the assumptions that sensor axes are perfectly orthogonal (it is therefore reasonable considering the typical small misalignments registered in the real accelerometers) and that the sensitivity of the three axes is the same. Under these assumptions, the third term in (3.16) can be rewritten as:

$$\frac{E\left[\left(\mathbf{S}^{-1}\mathbf{n}\right)^{\mathrm{T}}\mathbf{S}^{-1}\mathbf{n}\right]}{V_{CC}^2} \approx \frac{E\left[n_X^2/s*^2 + n_Y^2/s*^2 + n_Z^2/s*^2\right]}{V_{CC}^2}$$

$$= \frac{E\left[n_X^2\right] + E\left[n_Y^2\right] + E\left[n_Z^2\right]}{s*^2 V_{CC}^2}. \tag{3.18}$$

Each component of $\mathbf{n}$ is a Gaussian random variable with zero mean and variance σ^2: n_X, n_Y, $n_Z \sim \sigma \cdot G_1(1)$. The sum of k squared normal random variables is a χ^2 random variable with k degrees of freedom, indicated by χ_k^2; its mean is k and its variance is $2k$. Therefore, we can write:

$$\frac{E\left[\left(\mathbf{S}^{-1}\mathbf{n}\right)^{\mathrm{T}}\mathbf{S}^{-1}\mathbf{n}\right]}{V_{CC}^2} \approx \frac{\sigma^2}{s*^2 V_{CC}^2}\left(E\left[\chi_3^2\right]\right) = 3\frac{\sigma^2}{s*^2 V_{CC}^2}. \tag{3.19}$$

Substituting (3.17) and (3.19) into (3.16) we finally obtain:

$$E\left[\mathbf{a_n}^{\mathrm{T}}\mathbf{a_n}\right] \approx \left(\frac{\mathbf{v}}{V_{CC}} - \mathbf{o}\right)^{\mathrm{T}}\mathbf{S}^{-\mathrm{T}}\mathbf{S}^{-1}\left(\frac{\mathbf{v}}{V_{CC}} - \mathbf{o}\right) + 3\frac{\sigma^2}{s*^2 V_{CC}^2}$$

$$= \mathbf{a}^{\mathrm{T}}\mathbf{a} + 3\frac{\sigma^2}{s*^2 V_{CC}^2}. \tag{3.20}$$

This equation highlights that, in presence of noise on the measured sensor output, the squared length of the measured acceleration vector is biased by a factor which increases with the inverse of the squared sensor sensitivity, $1/s*^2$, and with the variance of the noise, σ^2.

This observation has some consequences for any application that requires the norm of the estimated acceleration vector to be considered, as the bias produced by noise has to be eliminated to avoid drifts. An example of this situation is illustrated in the following on a simple, didactic problem.

Fig. 3.2 Experimental setup
for estimating the radius R or
the angular speed ω of a
planar rotating disk, using an
accelerometer
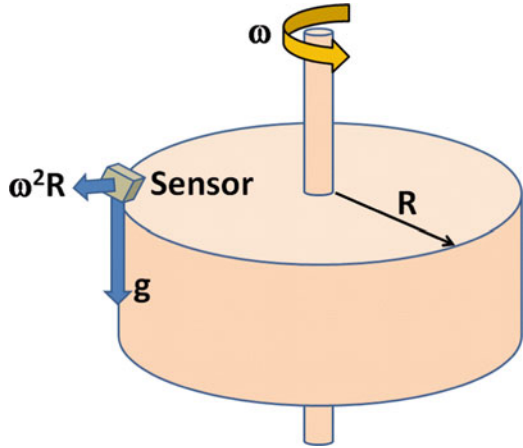
Let us suppose that a triaxial accelerometer is positioned at the border of a disk
of radius R, rotating at a constant angular speed ω (Fig. 3.2). Let us also suppose
that the sensor orientation is unknown. The sensor is subjected to the local gravity
force, **g**, in vertical direction, and to the centripetal force induced by the disk
rotation, which is radially oriented and has modulus equal to $\omega^2 R$. Since these
two forces are orthogonal to each other, the norm of the resultant acceleration
measured by the sensor should be equal to:

$$\|\mathbf{a}\| = \sqrt{g^2 + [\omega^2 R]^2}. \tag{3.21}$$

From (3.21), the radius R of the circle can be estimated from the module of the
acceleration measured by the accelerometer and ω; alternatively, the disk angular
speed ω may be derived from $\|\mathbf{a}\|$ and R, as:

$$\begin{cases} \omega = \sqrt{\dfrac{\sqrt{\|\mathbf{a}\|^2 - g^2}}{R}}, \\[4mm] R = \dfrac{\sqrt{\|\mathbf{a}\|^2 - g^2}}{\omega^2}. \end{cases} \tag{3.22}$$

It is evident, from (3.22), that to estimate R or ω, one has to reliably estimate
$\|\mathbf{a}\|^2$. However, in presence of noise, averaging the squared norm of the measured
acceleration vectors gives $\|\mathbf{a}\|^2 + 3\sigma^2/(s*^2 V_{CC}^2)$ in spite of $\|\mathbf{a}\|^2$; as a consequence,
ω and R will be both overestimated.

To give a more quantitative idea of this phenomenon, let us consider a disk of
radius $R = 25$ m, rotating at an angular speed $\omega = 0.01$ rad/s, corresponding at
about one rotation every 10 min. The resulting centripetal acceleration is equal to
$\omega^2 R = 0.0025$ m/s^2, orthogonal to the gravity force; assuming $g = 9.80665$ m/s^2,
the norm of the acceleration experimented by the sensor is equal to 9.80678 m/s^2.

Table 3.1 Main features of the two MEMS accelerometers considered here

Accelerometer	Range	Bandwidth [Hz]	V_{CC} [V]	$1/s*$ [m/s²]	o	σ^2 [V²]	$3\sigma^2/[s*^2 V_{CC}^2]$ [m²/s⁴]
ST LIS3L02AL	±2g	285	3.3	49.03	0.5	4.9658E − 07	0.000329
ADXL330 (Wii)	±3g	500	3	98.07	0.5	6.4800E − 06	0.020773

Table 3.2 Estimated radius, R, and angular speed, ω, of a rotating planar disk, using two different accelerometers, with and without correction of the noise bias

	R [m]	ω [rad/s]	Noise bias correction
True value	25.00000	0.10000	–
LIS3L02AL (ST)	25.04940	0.10010	No
ADXL330 (Wii)	28.80100	0.10733	No
LIS3L02AL (ST)	25.00510	0.10001	Yes
ADXL330 (Wii)	24.98460	0.09997	Yes

Let us consider then two typical triaxial MEMS accelerometers: the first one is the LIS3L02AL by ST Microelectronics [27], already analyzed in [4]; this is a high performance accelerometer for low frequency applications, characterized by low noise. The second sensor is the ADXL330 by Analog Devices [28], which is currently employed in the Wiimote controller by Nintendo [29]. The main characteristics of these sensors, taken from their datasheets and including the noise variance σ^2 and the corresponding noise bias, are summarized in Table 3.1.

Table 3.2 reports the values of R and ω estimated from 10,000,000 different values of $\|\mathbf{a}\|^2$ obtained through simulation. In particular, the correct value of $\mathbf{v}$ was generated for each sensor, and white Gaussian noise with variance σ^2 equal to that reported in Table 3.1 was added to the output channels of the accelerometers. The value of $\|\mathbf{a}\|^2$ in (3.16) was then estimated averaging 10,000,000 values of the squared norm of the acceleration. Notice that the values of R and ω are overestimated by both accelerometers; the second sensor, which is noisier than the first one, overestimates the disk radius by more than 10 %. However, if the bias introduced by the noise term is taken into account, R and ω are properly estimated.

Such results demonstrate that the bias introduced by noise can dramatically affect the estimates, especially when small accelerations are considered like in this case [30]. A typical application where such situation occurs in practice is breath controlling through accelerometers [31, 32]: in this case, an accelerometers is positioned onto the stomach of the subject and it has to measure the small accelerations induced by the breath process.

3.4 Local Gravity Variations

As already noted, the major part of the calibration procedures are generally based on the fact that, in static condition, the module of the acceleration vector measured by the sensor must equal the local acceleration gravity. This is generally assumed to

Table 3.3 This table shows the maximum drift induced by a 1 min integration of the accelerometer output, calibrated without considering the local gravity variations due to latitude, altitude, gravity anomaly and tidal effect. The drift effects induced by the noise bias are also reported

	Induced Δg, % (9.80665 m/s^2 = 100 %)	Induced Δg [m/s^2]	Position drift after 1 min [m]
Latitude	0.5300	0.05198	93.56
Altitude	0.2800	0.02746	49.43
Gravity anomaly	0.0100	0.00098	1.77
Tidal effect	0.0030	0.00029	0.53
$3\sigma^2/(s^{*2}V_{CC}^2)$, ST LIS3L02AL	0.0002	0.00002	0.03
$3\sigma^2/(s^{*2}V_{CC}^2)$, ADXL300 (Wii)	0.0108	0.00106	1.91

be $g = 9.80665$ m/s^2, that represents a mean value of the acceleration induced by the Earth gravity field. However, as noticed in [33, 34] or [5], and clearly illustrated in [35], different factors may contribute to modify the local value of g. These are the following:

1. *Latitude*—Because of the centrifugal force resulting from the rotation of the Earth, which is null at the poles and maximum at the equator, and also because of the bulge of the Earth at the equator, the value of the acceleration of gravity varies from 9.780 m/s^2 at the equator to 9.832 m/s^2 at the poles: a difference of 0.53 %.
2. *Altitude*—Since the gravitational force is proportional to the inverse of the square of the distance from the center of mass, the value of the acceleration of gravity varies with the altitude. Comparison of the acceleration of gravity measured at sea level and on the top of mount Everest shows a difference of about 0.28 %.
3. *Gravity anomaly*—The local gravity field is locally affected by the presence of mountains, canyons or concentration or low/high density rocks in the mantel. Typical variations are generally included in the interval ± 0.001 m/s^2, corresponding to a variation of 0.01 % of the nominal value of the acceleration gravity [36].
4. *Tidal effect*—Depending on the geometrical configuration of the Earth/moon/ sun system, the sun and moon gravitational mass attraction may induce temporary variations as large as 0.003 % of the local gravity force.

Most authors do not consider these factors during the calibration procedure. As a consequence, the estimated sensor sensitivity is over or underestimated, and drifts are introduced when the output of the accelerometers in an IMU is integrated over time to derive the position information. Table 3.3 shows the maximum drifts induced by these factors when the sensor output is integrated over 60s, and an average acceleration close to 10 m/s^2 is registered for such interval of time. The same table shows the drifts introduced by the noise bias (3.20) for the two types of sensor considered here.

This table dramatically demonstrates the need for correcting the value of g during calibration, at least for the variations induced by latitude and altitude. In fact, without such correction, the position drift can easily exceed 50 m after 1 min. The same table also demonstrates that gravity anomaly, tidal effect and bias introduced by noise are one or two orders of magnitude smaller and, at least in first approximation, they can be disregarded.

Fortunately, the influence of the first two main factors can be easily taken into account to get a reliable estimate of the local acceleration vector, as a function of the latitude and altitude. In particular, considering the radius of the Earth at the equator and at the poles (and assuming its shape as an ellipsoid), the mass of the planet and the centripetal force due to Earth rotation and the ellipsoidal shape of our planet, the *International Gravity Formula* has been derived [37]:

$$g(\theta) = 9.780327\left[1 + 5.3024 \times 10^{-3}\sin^2(\theta) - 5.8 \times 10^{-6}\sin^2(\theta)\right] \text{ m/s}^2, \quad (3.23)$$

which gives the value of the acceleration gravity, $g(\theta)$, as a function of the latitude, θ. For instance, at the equator (3.17) gives $g(0°) \approx 9.78$ m/s^2; at the poles, g ($\pm 90°$) ≈ 9.83 m/s^2; whereas at 45° latitude, it gives $g(\pm 45°) \approx 9.81$ m/s^2.

Altitude can be taken into account considering that the mass attraction decreases with the square of the distance from the mass center. Linearization of this relation around the sea level gives raise to the *Free Air Correction* formula; the gravity force decreases approximately of 0.000003086 m/s^2 per meter height; once included into (3.23), this gives:

$$g(\theta, h) = 9.780327\left[1 + 5.3024 \times 10^{-3}\sin^2(\theta) - 5.8 \times 10^{-6}\sin^2(\theta)\right]$$
$$- 3.086 \times 10^{-6}h \text{ m/s}^2, \quad (3.24)$$

where h is the height (in meters) with respect to the sea level.

Equation (3.24) provides a simple way to compute the local value of the acceleration of gravity depending on the latitude and altitude; such computation should always be performed before starting any sensor calibration procedure, as an inaccurate estimation of the gravity acceleration corrupts the estimate of the sensor sensitivity and, as a consequence, may introduce drifts over the integrated signal which easily overcomes 50 m after 1 min. An alternative to use of (3.24) is measuring the local gravity field through a gravimeter. However, this solution is time consuming and costly; it is preferable for most applications to approximate it with (3.24).

3.5 Calibration Procedures

Calibration procedures are aimed at estimating the offset, sensitivity and axis misalignments of the sensor. More precisely, the inverse sensitivity matrix, $\mathbf{S}^{-1}$, and the offset vector, $\mathbf{o}$, in (3.15), are generally estimated, as these permit to

directly transform the output of the sensor, in V, into an acceleration vector, given in m/s^2, as in (3.15).

Most of the calibration procedures are based on the fact that, in static conditions, the module of the acceleration vector measured by the sensor must equal the local acceleration gravity, g. As noted before, most authors assume $g = 9.80665$ m/s^2 independently from latitude and altitude. However, to avoid a biased estimate of the sensitivity parameters, it is reasonable to use (3.24) to get an accurate prediction of g, after that the calibration procedure can be performed.

The accelerometer calibration procedures are divided into different families, that are briefly analyzed in the following [13]: the *six-positions method*, the *extended six-positions method* and the *autocalibration* procedures; a brief description of some alternative calibration procedures is also provided at the end of the paragraph. More space is dedicated to the description of the autocalibration procedure that constitutes the most cost effective and reliable solution, and it is therefore widely adopted.

3.5.1 Six-Positions Method

This kind of calibration procedure is based on six orthogonal measurements of the gravity force vector. It is therefore capable to estimate the parameters of a sensor model with at most six unknowns that represent the sensor offsets and sensitivities along the three axes. On the other hand, axis misalignment cannot be estimated.

For each measurement of gravity, the sensor should be ideally oriented such that one of its axes is aligned with respect to the gravity force. For each axis, the offset and sensitivity are then derived from (3.2); in fact, for the X axis, we can for instance write the following equations:

$$\begin{cases} v_{X,1} = V_{CC}(s_X g + o_X), \\ v_{X,2} = V_{CC}(-s_X g + o_X), \end{cases} \tag{3.25}$$

where $v_{X,1}$ and $v_{X,2}$ are the measured outputs of the X channel when the sensor's X axis is respectively parallel and antiparallel with respect to the gravity force. Solving (3.25) leads to the estimate of s_X, o_X.

This calibration procedure is characterized by the simplicity of its implementation: each axis can be calibrated independently from the others and this only requires solving a linear system with two equations and two unknowns. Nevertheless, the procedure has some critical drawbacks. First of all, it requires to use a costly machinery to accurately position the sensor into six different orientations, each orthogonal to the others; however, since the sensor package hides the internal structure, it is not possible to guarantee that the sensor is properly oriented with respect to the calibration bank; therefore, a global misalignment of the sensor can

result. Moreover, the procedure is time consuming and does not allow estimating the misalignment between the axes.

Calibrating an accelerometer with the six-position method is therefore limited to low-accuracy applications, like for instance in [23], where a low precision seismograph is described, or in [19], where the only norm of the acceleration vector is used to quantify the physical activity of a human subject. For lower precision applications, like in the case of the Wiimote controller [29], the sensor calibration can even be performed without resorting to a costly rotating bank, but simply rotating by hand the sensor into six "almost" orthogonal positions; in this case, the six-position method results in a simple, fast and poorly accurate calibration method.

3.5.2   Extended Six-Positions Method

Many authors perform a sequence of at least nine measurements, with controlled sensor orientations, to obtain the calibration data [16, 30]. This allows estimating not only the offset and sensitivity of each axis, but also the axis misalignments and, in some cases, the sensor nonlinearity [16] and the noise properties [30].

Different authors use the controlled calibration data in different manners to obtain different calibration strategies. In [30], a sensor model including offsets, sensitivities, axes misalignments and non linearities is considered; moreover, wavelets are used to analyze the output signal of the accelerometers in the time-frequency domain; this allows for estimating the typical noise characteristics and developing a soft thresholding method which is used to eliminate the wavelet components associated to the noise from the signal.

In [16], a model including offsets, sensitivities, axes misalignments and nonlinearity is considered; calibration is performed measuring the acceleration at different orientations with respect to gravity, while one sensor axis is aligned horizontally; a turn-table is used to this aim. The sensor parameters are then estimated minimizing a cost function which is composed of the sum of two terms: the first term represents the fact that the sensor output must be zero for the horizontal sensing axis; the second term takes into account that the norm of the measured acceleration must equal g; a scalar parameter is also included to assign different weights to the two costs. Based on their results, the authors suggest avoiding the use of non linear models, as the parameters describing the non linearities cannot be reliably estimated.

Overall, the extended six-positions method presents some advantages with respect to the six-position method, as it allows adopting more complex sensor models. However, this kind of calibration can only be performed in a controlled environment, using costly machinery and a time consuming procedure.

3.5.3 Autocalibration Methods

Autocalibration methods are the most used [4, 9–11, 13, 15, 25, 38]; the only assumption required is that, in static conditions, the module of the acceleration vector measured by the sensor equals the local acceleration gravity, g. From this and from a sequence of acquisitions performed at random orientations, the parameters of the sensor model are estimated. Simple sensor models with only one offset and sensitivity parameters as well as complex models including nonlinearity can be adopted in autocalibration. However, the most diffused choice is represented by the nine parameters model including three offsets, three sensitivities and three cross axis terms.

More precisely, autocalibration is based on the minimization of a cost function, representing the sum of the differences between the norm of the measured accelerations and g, as a function of the model parameters. Slightly different cost functions are however adopted by different authors, leading to more or less complex minimization strategies. In [13], a weighted least squares scheme is adopted to compare the squared norm of the measured accelerations with g^2; the linearization of the cost function leads to a constrained minimization which is generally achieved by a proper iterative algorithm in less than 30 iterations. On the other hand, in [9] a very simple sensor model including only one offset and one sensitivity parameter is adopted. This allows minimizing the cost function (and therefore estimating the model parameters) in closed form. In [15], as in [4, 11, 25] a cost function in the form:

$$E(\theta) = \sum_{i=1}^{N} \left(\left\| \mathbf{a}_{\mathbf{i},\theta} \right\|^2 - g^2 \right)^2 \tag{3.26}$$

is adopted, where $\boldsymbol{\theta}$ is the vector of the model parameters and N is the number of measured acceleration vectors. Such cost function is characterized by the fact that only the squared norm of the measured accelerations appears in it; therefore, it can be minimized through efficient iterative algorithms like the Newton's method [4].

The success of autocalibration procedures is explained by the fact that they do not require any special machinery to be performed, and they are therefore extremely cheap and easy to perform; they only require the sensor to be randomly oriented a sufficient number of times, covering the whole range of orientations and measuring each time the module of the static acceleration, and the minimization of a cost function. For this reason, autocalibration can even be performed on-line: for instance, in [9], each time a period of sensor immobility is detected, the modulus of the gravity force is measured and the sensor parameters are updated. In this manner, changes of the sensor sensitivity due, for instance, to changes of temperature, can easily be managed and corrected in real time.

In spite of the large literature on autocalibration methods, only one author [25], between the ones cited here, has spent some words about the adequacy of the cost function with respect to the sensor noise model. Here we therefore propose an original derivation of the cost function in the context of the maximum likelihood

estimate, starting from the sensor noise model described by (3.15). Coherently with the other autocalibration procedures, we will assume that, in static condition, the sensor is subjected only to the force of gravity, whose local intensity g can be computed through (3.24). To derive a simpler cost function, similarly to what done in [4, 11, 15, 25], we will finally consider the squared norm of the measured acceleration vector (like in (3.26)) instead of the simple norm.

Let us consider therefore a set of N acceleration vectors, measured in static condition. The squared norm of the noisy gravity acceleration vector, $\mathbf{g_n}$, measured by the sensor, is given by:

$$
\begin{aligned}
\mathbf{g_n^T g_n} &= \left\{ \mathbf{S}^{-1} \left(\frac{\mathbf{v} - \mathbf{n}}{V_{CC}} - \mathbf{o} \right) \right\}^T \mathbf{S}^{-1} \left(\frac{\mathbf{v} - \mathbf{n}}{V_{CC}} - \mathbf{o} \right), \\
&= \left(\frac{\mathbf{v}}{V_{CC}} - \mathbf{o} \right)^T \mathbf{S}^{-T} \mathbf{S}^{-1} \left(\frac{\mathbf{v}}{V_{CC}} - \mathbf{o} \right) - 2\mathbf{n}^T \frac{\mathbf{S}^{-T}}{V_{CC}} \mathbf{S}^{-1} \left(\frac{\mathbf{v}}{V_{CC}} - \mathbf{o} \right) + \frac{\mathbf{n}^T \mathbf{S}^{-T} \mathbf{S}^{-1} \mathbf{n}}{V_{CC}^2}, \\
&= \mathbf{g}^T \mathbf{g} - 2\mathbf{n}^T \frac{\mathbf{S}^{-T}}{V_{CC}} \mathbf{g} + \frac{\mathbf{n}^T \mathbf{S}^{-T} \mathbf{S}^{-1} \mathbf{n}}{V_{CC}^2}.
\end{aligned}
\tag{3.27}
$$

The first term in (3.27) is constant and equal to g^2. To analyze the second term in (3.27), let us consider a sensor with perfectly aligned axes with equal sensitivity and offset; let us assume that $1/s*$ is the inverse sensitivity of each axis. When this ideal sensor is randomly oriented in the space and measures an acceleration of intensity g, this term reduces to:

$$
2\mathbf{n}^T \frac{\mathbf{S}^{-T}}{V_{CC}} \mathbf{g} \rightarrow 2 \frac{g}{s * V_{CC}} \mathbf{n}^T \mathbf{m},
\tag{3.28}
$$

where $\mathbf{m}$ is a random 3×1 versor. The term $g\mathbf{m}$ represents the gravity acceleration in the sensor reference frame: as the sensor is randomly oriented, also the measured acceleration has a random orientation. Notice now that, since $\mathbf{m}$ is a versor, $\mathbf{n}^T \mathbf{m}$ is a linear combination of three Gaussian random variables with variance σ^2, and the squared mixing coefficients sum to one ($\mathbf{m}^T \mathbf{m} = 1$); therefore, $\mathbf{n}^T \mathbf{m}$ itself is a Gaussian random variable with variance σ^2. Overall, the second term in (3.27) results to be a Gaussian random variable with zero mean and variance equal to $[2g\sigma/(s*V_{CC})]^2$.

For the same ideal sensor, the third term in (3.27) is a random variable with approximate distribution $[\sigma^1/(s*V_{CC})]^2 \chi_3^2$; this has a mean value of $3[\sigma/(s*V_{CC})]^2$ and variance equal to $6[\sigma/(s*V_{CC})]^4$.

Table 3.4 show the average and variance of the three terms in (3.27), for the two accelerometers considered here. Since the variance of the third term is typically very small with respect to the variance of the second term, we assume that the third term contributes only with its mean value to $\mathbf{g_n}^T \mathbf{g_n}$. As a consequence, we can approximate $\mathbf{g_n}^T \mathbf{g_n}$ with a Gaussian random variable, that is $\mathbf{g_n}^T \mathbf{g_n} \sim g^2 + 3[\sigma/(s*V_{CC})]^2 + G_1(3[2g\sigma/(s*V_{CC})]^2)$. The maximum likelihood

Table 3.4 The average and the variance for the three terms of g^Tg in (3.27) are reported here for two typical MEMS triaxial accelerometers

		LIS3L02AL (ST)	ADXL330 (Wii)
$(\mathbf{v}/V_{CC} - \mathbf{o})^T\mathbf{S}^{-T}\mathbf{S}^{-1}(\mathbf{v}/V_{CC} - \mathbf{o})$	Average [m/s^2]	9.80665	9.80665
	Variance [m^2/s^4]	0	0
$2\mathbf{n}^T/V_{CC}\mathbf{S}^{-T}\mathbf{S}^{-1}(\mathbf{v}/V_{CC} - \mathbf{o})$	Average [m/s^2]	0	0
	Variance [m^2/s^4]	4.2174E − 02	2.66364
$\mathbf{n}^T\mathbf{S}^{-T}\mathbf{S}^{-1}\mathbf{n}/V_{CC}^2$	Average [m/s^2]	3.2890E − 04	2.0772E − 02
	Variance [m^2/s^4]	7.21180E − 08	2.8767E − 04

estimate of the sensor model parameters $\boldsymbol{\theta}$ from a set of N measurements corrupted by Gaussian noise is obtained by the least squares estimate; the cost function to be minimized (corresponding to the negative log likelihood) is therefore given by:

$$E(\theta) = \sum_{i=1}^{N}\left[\|\mathbf{a}_{i,\theta}\|^2 - \left(g^2 + 3\frac{\sigma^2}{s^{*2}V_{CC}^2}\right)\right]^2. \tag{3.29}$$

Such reasoning line justifies the choice of a quadratic cost function operated, for instance, in [4, 11, 25]. With respect to these, however, we have introduced in (3.29) the term $3[\sigma/(s*V_{CC})]^2$, which takes into account the bias introduced by the quadratic noise term.

Choosing the traditional sensor model with nine parameters, including three offsets, three sensitivity and the axes misalignments, (3.29) is rewritten as:

$$E(\mathbf{o},\mathbf{S^{-1}}) = \sum_{i=1}^{N}\left[\left(\frac{\mathbf{v_{n,i}}}{V_{CC}} - \mathbf{o}\right)^T\mathbf{S}^{-T}\mathbf{S}^{-1}\left(\frac{\mathbf{v_{n,i}}}{V_{CC}} - \mathbf{o}\right) - \left(g^2 + 3\frac{\sigma^2}{s^{*2}V_{CC}^2}\right)\right]^2, \tag{3.30}$$

where $\mathbf{v_{n,i}}$ is the noisy sensor output measured at the ith orientation, and $\mathbf{S}$ (and therefore also $\mathbf{S}^{-1}$) is assumed to be symmetric as in [4]. As already noticed, the autocalibration procedure does not estimate $\mathbf{S}$ directly, but it estimates $\mathbf{S}^{-1}$; from this, $\mathbf{S}$ is then easily derived by matrix inversion. Notice, however, that (3.30) is not linear with respect to the elements of $\mathbf{S}^{-1}$ and $\mathbf{o}$. A closed solution for the minimization of $E(\mathbf{o}, \mathbf{S}^{-1})$ is not available: an iterative minimization algorithm has to be employed to this aim. To the scope, we have adopted the Newton's method, which is an iterative optimization procedure that guarantees quadratic convergence towards the solution [39]. Starting from an initial guess of the sensor parameters, which is reasonably the one provided by the sensor manufacturer in the datasheet, the solution is iteratively updated as:

$$\boldsymbol{\theta^{t+1}} = \boldsymbol{\theta^t} - \alpha\mathbf{H^{-1}}(\boldsymbol{\theta^t}) \cdot \mathbf{J}(\boldsymbol{\theta^t}), \tag{3.31}$$

where $\boldsymbol{\theta}^{\mathbf{t}} = [\theta_1, \theta_1, \ldots, \theta_9] = [o_X, o_Y, o_Z, S^{-1}{}_{XX}, S^{-1}{}_{YY} S^{-1}{}_{ZZ} S^{-1}{}_{XY} S^{-1}{}_{XZ} S^{-1}{}_{YZ}]$ is the unknown vector parameters at the tth iteration, containing the offset vector $\mathbf{o}$ and the six independent elements of $\mathbf{S}^{-1}$. The terms $\mathbf{J}(\boldsymbol{\theta}^{\mathbf{t}})$ and $\mathbf{H}(\boldsymbol{\theta}^{\mathbf{t}})$ in (3.31) are the Jacobian vector and the Hessian matrix of the cost function $E(\boldsymbol{\theta})$, defined respectively as follows:

$$\mathbf{J}(\theta^{\mathbf{t}}) = \left[\frac{\partial E}{\partial \theta_1}, \frac{\partial E}{\partial \theta_2}, \ldots, \frac{\partial E}{\partial \theta_9} \right], \quad \mathbf{H}(\theta^{\mathbf{t}}) = \left\{ h_{ij} = \frac{\partial^2 E}{\partial \theta_i \partial \theta_j} \right\}_{i,j=1\ldots9}, \qquad (3.32)$$

α is a damping parameter ($0 < \alpha < 1$) and it is computed at each iteration by means of a line search procedure [39].

Notice that, since the cost function (3.30) is a sum of squared terms, the derivatives in (3.31) and (3.32) can be easily computed from the following definitions:

$$\begin{cases} \boldsymbol{\theta} = \left(\mathbf{o}, \mathbf{S}^{-1} \right), \\ \varepsilon_i(\boldsymbol{\theta}) = \left(\frac{\mathbf{v_{n,i}}}{V_{CC}} - \mathbf{o} \right)^{\mathrm{T}} \mathbf{S}^{-\mathrm{T}} \mathbf{S}^{-1} \left(\frac{\mathbf{v_{n,i}}}{V_{CC}} - \mathbf{o} \right) - \left(g^2 + 3 \frac{s_{-1}^2 \sigma^2}{V_{CC}^2} \right), \\ E(\boldsymbol{\theta}) = \sum_{i=1}^{N} \varepsilon_i{}^2(\boldsymbol{\theta}) = \varepsilon(\boldsymbol{\theta})^{\mathrm{T}} \varepsilon(\boldsymbol{\theta}), \\ \frac{\partial E}{\partial \theta_j} = 2 \sum_{i=1}^{N} \varepsilon_i(\boldsymbol{\theta}) \frac{\partial \varepsilon_i(\boldsymbol{\theta})}{\partial \theta_j}, \\ \frac{\partial^2 E}{\partial \theta_j \partial \theta_k} = \frac{\partial^2 E}{\partial \theta_k \partial \theta_j} = 2 \sum_{i=1}^{N} \left(\frac{\partial \varepsilon_i(\boldsymbol{\theta})}{\partial \theta_j} \frac{\partial \varepsilon_i(\boldsymbol{\theta})}{\partial \theta_k} + \varepsilon_i(\boldsymbol{\theta}) \frac{\partial^2 \varepsilon_i(\boldsymbol{\theta})}{\partial \theta_j \partial \theta_k} \right).. \end{cases} \qquad (3.33)$$

Iterations are stopped when the following convergence criterion is satisfied:

$$\max_{i=1\ldots9} \left\{ \left| \frac{\theta_i^t - \theta_i^{t-1}}{(\theta_i^t + \theta_i^{t-1})/2} \right| \right\} < \delta, \qquad (3.34)$$

where δ is a threshold, which has empirically been set equal to 1.5×10^{-6} to guarantee that the estimated parameters assume stable values. Such criterion expresses the fact that the maximum change of a model parameter between two consecutive iterations does not exceed 0.00015 %. Despite this strong convergence criterion, and thanks to the high convergence rate achieved by the Newton's method, less than ten iterations are generally sufficient to converge. Two typical calibration results obtained with this autocalibration procedure are described in the next pages, where the problem of estimating the accuracy of the computed model parameters is also assessed.

3.5.4 Other Calibration Methods

Several other calibration methods, although less diffused, have been proposed in literature. Some of them, like those in [40, 41], avoid explicit measurements of the sensor output, since they are based only on electrical tests, and they generally permit to estimate the full frequency response of the sensor. They can however be performed only in laboratory, using the proper electrical equipment. Other calibration methods, like that proposed in [14], include the dependency of the sensor parameters from temperature; also these require special equipments and can be performed only in laboratory.

3.6 Results

In this section we illustrate the typical results of an autocalibration procedure, based on the minimization of the cost function (3.30). We also present a methodology to evaluate the sensor accuracy after calibration, based on comparing the MEMS measurements with those obtained by a commercial motion capture system (SMART3D™ [42]). This also allows comparing the six parameters sensor model (3.2) with the nine parameters model, and to demonstrate the superiority of the last one. It also serves to highlight the dramatic increase of accuracy registered after the sensor is calibrated, and therefore the need for calibration.

The results are referred to the LIS3L02AL triaxial accelerometer by ST, whose main characteristics are reported in Tables 3.1 and 3.5. Four different accelerometers of this kind were considered in this study. The output of the MEMS accelerometers were acquired by a host computer at a sampling rate of 960 Hz through a NI-DAQ board. An analog low-pass RC filter was added to the accelerometer output to filter high frequency noise and avoid aliasing, which would have been introduced by sampling. The bandwidth of the filter was set to 285 Hz, which is large enough, for instance, for tracking the human finest movements [4, 43].

The sensors were calibrated using a different number of sensor random orientations, ranging from $N = 72$ for the sensor #1, to $N = 42$ for the sensor #2 and $N = 35$ for sensors #3 and #4. The parameters of the bias vector, $\mathbf{o}$, and of the inverse sensitivity matrix, $\mathbf{S}^{-1}$, are reported in Tables 3.6, 3.7 and 3.8 for each of the four accelerometers.

Table 3.5 Some of the most significant parameters of the LIS3L02AL MEMS accelerometer

Parameter	Value	Unit
Zero-g level	$V_{CC}/2 \pm 6\ \%$	V
Bias drift vs. temperature	$\pm 1.47 \times 10^{-2}$	$m/(s^2\ ^\circ C)$
Acceleration range	± 20	m/s^2
Sensitivity	$V_{CC}/49 \pm 10\ \%$	$V/(m/s^2)$
Cross-axis	± 2	% of sensitivity
Acceleration noise density	5×10^{-4}	$m/(s^2\ \sqrt{Hz})$

Table 3.6 Estimated values of the components of the bias vector, with estimated standard deviation. The nominal value is 0.5 for both the LISL02AL and ADXL330 sensors

		o_X	o_Y	o_Z
LIS3L02AL (ST) #1	Estimated value	0.49153	0.48619	0.54819
	Std	$1.31E - 06$	$2.87E - 06$	$1.50E - 06$
	Std %	0.00027 %	0.00059 %	0.00027 %
LIS3L02AL (ST) #2	Estimated value	0.52071	0.49948	0.51016
	Std	$3.54E - 06$	$1.02E - 05$	$5.25E - 06$
	Std %	0.00068 %	0.00204 %	0.00103 %
LIS3L02AL (ST) #3	Estimated value	0.42085	0.49741	0.49981
	Std	$2.05E - 05$	$9.91E - 06$	$4.59E - 06$
	Std %	0.00488 %	0.00199 %	0.00092 %
LIS3L02AL (ST) #4	Estimated value	0.45424	0.52032	0.45312
	Std	$2.50E - 05$	$9.84E - 06$	$5.09E - 06$
	Std %	0.00549 %	0.00189 %	0.00112 %
ADXL330 (AD—Wii)	Estimated value	0.49248	0.48815	0.49163
	Std	$2.59E - 05$	$1.79E - 05$	$1.82E - 05$
	Std %	0.00525 %	0.00366 %	0.00371 %

Table 3.7 Estimated values of the diagonal elements of the inverse sensitivity matrix, with estimated standard deviation. The nominal value is 49.05 m/s^2 for the LISL02AL sensor, and 98.1 m/s^2 for the ADXL330 sensor

		S^{-1}_{XX} (m/s^2)	S^{-1}_{YY} (m/s^2)	S^{-1}_{ZZ} (m/s^2)
LIS3L02AL (ST) #1	Estimated value	50.02726	50.47767	51.38764
	Std	$3.71E - 04$	$9.57E - 04$	$3.63E - 04$
	Std %	0.00074 %	0.00190 %	0.00071 %
LIS3L02AL (ST) #2	Estimated value	49.50062	50.94925	49.61606
	Std	$8.52E - 04$	$3.33E - 03$	$1.15E - 03$
	Std %	0.00172 %	0.00654 %	0.00232 %
LIS3L02AL (ST) #3	Estimated value	53.24319	53.99703	48.29837
	Std	$6.62E - 03$	$2.58E - 03$	$1.23E - 03$
	Std %	0.01244 %	0.00478 %	0.00255 %
LIS3L02AL (ST) #4	Estimated value	51.21930	51.96574	47.13613
	Std	$7.63E - 03$	$2.50E - 03$	$1.46E - 03$
	Std %	0.01490 %	0.00482 %	0.00309 %
ADXL330 (AD—Wii)	Estimated value	97.74048	97.21622	99.36618
	Std	$3.39E - 02$	$2.22E - 02$	$2.24E - 02$
	Std %	0.03469 %	0.02281 %	0.02253 %

Notice that the computed values may significantly differ from the nominal ones: for instance, the bias of the X channel of the accelerometer #3 is 16 % smaller than its nominal value (Table 3.6), whereas the inverse sensitivity of the Y channel of the same accelerometer is 10 % larger than its nominal value (Table 3.7).

Table 3.8 Estimated values of the off-diagonal elements of the inverse sensitivity matrix, with standard deviation. The nominal value is 0 for both the LISL02AL and ADXL330 sensors

		S^{-1}_{XY} (m/s^2)	S^{-1}_{XZ} (m/s^2)	S^{-1}_{YZ} (m/s^2)
LIS3L02AL (ST) #1	Estimated value	-0.38794	0.22297	0.01980
	Std	$3.56E - 04$	$3.26E - 04$	$4.58E - 04$
	Std %	0.09186 %	0.14610 %	2.31562 %
LIS3L02AL (ST) #2	Estimated value	-0.52038	-0.17683	0.07647
	Std	$1.01E - 03$	$6.88E - 04$	$1.49E - 03$
	Std %	0.19354 %	0.38900 %	1.94430 %
LIS3L02AL (ST) #3	Estimated value	1.25742	1.44731	0.59025
	Std	$2.27E - 03$	$1.15E - 03$	$8.70E - 04$
	Std %	0.18082 %	0.07972 %	0.14744 %
LIS3L02AL (ST) #4	Estimated value	-0.58641	-0.35658	-0.24576
	Std	$2.43E - 03$	$1.22E - 03$	$8.70E - 04$
	Std %	0.41446 %	0.34336 %	0.35410 %
ADXL330 (AD—Wii)	Estimated value	-1.37789	0.02840	0.06594
	Std	$1.92E - 02$	$2.04E - 02$	$1.96E - 02$
	Std %	1.39585 %	71.79472 %	29.74861 %

3.6.1 Accuracy of the Estimated Sensor Parameters

Notice that, in Tables 3.6, 3.7 and 3.8, beyond the estimated parameter values, we also reported the estimated standard deviation for each parameter. This information is crucial to determine the reliability of the estimated parameters. As a matter of fact, a large standard deviation would indicate that the parameter cannot be accurately estimated, and therefore, it should be eliminated from the sensor model. To assess the reliability of the parameter estimate, a widely used solution in the statistical domain is employed to derive an estimate of the variability of the parameters from the estimated variance of the measurements. The accuracy on the estimated parameters is therefore evaluated through the covariance analysis [44], carried out on the linearized version of the cost function (3.30) around the final value of the parameters. More in details, we will illustrate in the following how this analysis can be performed, starting from the case of a linear least squares system, and extending then the theory to the case of a nonlinear system.

Let us suppose that measurements are affected by additive Gaussian noise, zero mean, and with variance, σ_0^2, that is often called sample standard deviation. Let us also suppose that noise is independent on the different samples. This information is often available from the knowledge of the measurement process.

In our case, in particular, the sensor noise is provided in the sensor datasheet; the expected noise on the norm of the squared acceleration vector can be derived from the computed sensor parameters and (3.27); more in detail, we have demonstrated that such noise can be reasonably assumed to be Gaussian, with variance σ_0^2 approximately equal to $[2g\sigma/(s^*V_{CC})]^2$.

In this case any linear model that relates a vector of parameters, $\mathbf{x}$, to a vector of measurements, $\mathbf{b}$, can be written in matrix form as:

$$\mathbf{Ax} = \mathbf{b} + \boldsymbol{\nu}, \tag{3.35}$$

where $\mathbf{A}$ is the design matrix and $\boldsymbol{\nu}$ is a vector containing the measurement error for each sample.

System (3.35) is solved in the least squares sense; this produces the maximum likelihood estimate of the parameters as:

$$\mathbf{x} = \left(\mathbf{A}^{\mathrm{T}}\mathbf{A}\right)^{-1}\mathbf{A}^{\mathrm{T}}\mathbf{b}. \tag{3.36}$$

We are interested in having an estimate of the reliability in the estimate of $\mathbf{x}$ and the correlation between a pair of parameters. To this purpose, let us analyze the effect of the residual $\boldsymbol{\nu}$ on the estimated parameters $\mathbf{x}$:

$$\mathbf{x} + \mathbf{u} = \mathbf{CA}^{\mathrm{T}}(\mathbf{b} + \boldsymbol{\nu}), \tag{3.37}$$

where $\mathbf{C} = (\mathbf{A}^{\mathrm{T}}\mathbf{A})^{-1}$ is called the covariance matrix and $\mathbf{u}$ is the error on the estimated parameters introduced by a measurement error $\boldsymbol{\nu}$. We therefore easily derive:

$$\mathbf{u} = \mathbf{CA}^{\mathrm{T}}\boldsymbol{\nu}. \tag{3.38}$$

Given the hypothesis on $\boldsymbol{\nu}$, the vector $\mathbf{u}$ is zero mean; in fact:

$$E[\mathbf{u}] = E\left[\mathbf{CA}^{\mathrm{T}}\boldsymbol{\nu}\right] = \mathbf{CA}^{\mathrm{T}}E[\boldsymbol{\nu}] = \mathbf{0}. \tag{3.39}$$

This means that the estimate of $\mathbf{x}$ is not biased. We can now compute the variability of $\mathbf{u}$, by evaluating:

$$E\left[\mathbf{uu}^{\mathrm{T}}\right] = E\left[\mathbf{CA}^{\mathrm{T}}\boldsymbol{\nu}\left(\mathbf{CA}^{\mathrm{T}}\boldsymbol{\nu}\right)^{\mathrm{T}}\right] = E\left[\mathbf{CA}^{\mathrm{T}}\boldsymbol{\nu}\boldsymbol{\nu}^{\mathrm{T}}\mathbf{AC}^{\mathrm{T}}\right], \tag{3.40}$$

where the only term that has a statistical distribution is $\boldsymbol{\nu}$ and therefore (3.39) can be rewritten as:

$$E\left[\mathbf{uu}^{\mathrm{T}}\right] = \mathbf{CA}^{\mathrm{T}}E\left[\boldsymbol{\nu}\boldsymbol{\nu}^{\mathrm{T}}\right]\mathbf{AC}^{\mathrm{T}}. \tag{3.41}$$

Given the hypothesis of independence and Gaussianity of $\boldsymbol{\nu}$, $E[\boldsymbol{\nu}\,\boldsymbol{\nu}'] = \sigma_0{}^2\mathbf{I}$ and we obtain:

$$E\left[\mathbf{uu}^{\mathrm{T}}\right] = \mathbf{CA}^{\mathrm{T}}\mathbf{I}\sigma_0^2\mathbf{AC}^{\mathrm{T}} = \sigma_0^2\mathbf{CA}^{\mathrm{T}}\mathbf{AC}^{\mathrm{T}} = \sigma_0^2\mathbf{CC}^{-1}\mathbf{C}^{\mathrm{T}} = \sigma_0^2\mathbf{C}^{\mathrm{T}}. \tag{3.42}$$

The variance on the estimated parameters is therefore proportional to σ_0^2 and depends exclusively on the covariance matrix **C** (note that $\mathbf{C}^T = \mathbf{C}$):

$$\text{Var}[u_i] = \sigma_0^2 C_{ii}. \tag{3.43}$$

More generally, it can be demonstrated that the covariance between the ith and the jth elements of **u** is given by C_{ij}. The relationship between two parameters can then be expressed through the correlation index r_{ij}, which is computed as:

$$-1 \leq r_{ij} = \frac{E[u_i u_j]}{\sqrt{E[u_i u_i]E[u_j u_j]}} = \frac{C_{ij}}{\sqrt{C_{ii}C_{jj}}} \leq 1. \tag{3.44}$$

In the present situation, the relationship between the measurements (the voltage output vector **v**) and the model parameters ($\mathbf{S}^{-1}$ and **o**) is obtained through the nonlinear cost function (3.30). However, the here above derivation can still be applied linearizing (3.30) around the actual value of the parameters. In this case, the coefficient matrix **A** in (3.35) corresponds to the Jacobian matrix of $E(\mathbf{o}, \mathbf{S}^{-1})$ in (3.30), that is $\partial \boldsymbol{\varepsilon}(\boldsymbol{\theta})/\partial \boldsymbol{\theta}$ [see (3.33)]; the matrix **A** describes how a change of the estimated parameter vector, $\boldsymbol{\theta}$ [corresponding to **x** in (3.35)] influences the error vector, $\boldsymbol{\varepsilon}(\boldsymbol{\theta})$. More precisely, such relation is given by $\partial \boldsymbol{\varepsilon}(\boldsymbol{\theta})/\partial \boldsymbol{\theta} \cdot \Delta \boldsymbol{\theta} \approx \boldsymbol{\varepsilon}(\boldsymbol{\theta} - \Delta \boldsymbol{\theta}) - \boldsymbol{\varepsilon}(\boldsymbol{\theta})$, where the right term of the equation corresponds to $\mathbf{b} + \boldsymbol{\nu}$ in (3.35), and it represents a vector where each component has a Gaussian distribution with variance equal to $\sigma_0^2 = [2g\sigma/(s^*V_{CC})]^2$. Therefore, (3.43) still provides an estimate of the error in the computation of the parameters.

As it can be appreciated in Table 3.6, the estimation uncertainty for the bias vector is always lower than 0.006 % for the ST accelerometer; this means that **o** is estimated with great precision by the calibration procedure. For the diagonal elements of $\mathbf{S}^{-1}$, the standard deviation never exceeds 0.015 %: also these parameters are accurately estimated. The standard deviation for the off-diagonal elements of $\mathbf{S}^{-1}$ reaches 2.32 % of its nominal value in the worst case: this term are estimated with a less, but still reasonable, accuracy.

3.6.2 Evaluation of the Accuracy of the Calibrated Sensor Used as a Tilt Sensor

Once the autocalibration procedure has been completed, the accelerometer is ready to be used. We first observe that, when used as a tilt sensor, the orientation of the sensor in 3D space can be defined by only two angles (ρ and φ in Fig. 3.3), which represent the orientation of the device with respect to the gravity vector, **g**: the rotation around an axis parallel to **g** cannot be observed since the sensor output is invariant for rotations around such axis.

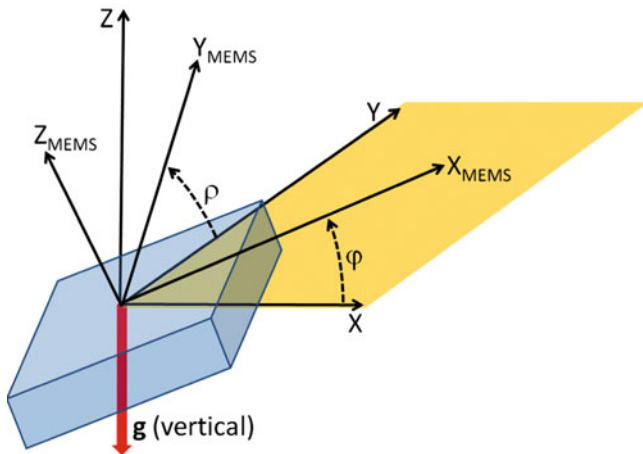**Fig. 3.3** The angles φ and ρ, which describe the orientation of the sensor accelerometer with respect to an absolute reference system having the Z axis oriented parallel to the gravity vector. The local reference system is indicated by the axes X_{MEMS}, Y_{MEMS}, Z_{MEMS} (© 2009 IEEE, reprinted with permission)

Let us define an absolute reference frame with the Z axis parallel to **g**. Let us indicate as (φ, ρ) the angles between the X and Y axes of the sensor and the horizontal plane (Fig. 3.3). From the acceleration vector obtained inverting (3.7), the angles φ and ρ could be computed by means of the following equations:

$$\begin{cases} \phi = \arcsin(a_X), \\ \rho = \arcsin(a_Y). \end{cases} \tag{3.45}$$

These equations are frequently used with biaxial accelerometers, but they suffer from a critical drawback: the sensitivity on the estimated values of φ and ρ depends on the value of φ and ρ itself, as shown in Fig. 3.4 and already highlighted by some but not all authors (see for instance [4, 5, 33]). To overcome this problem, the following trigonometric equations can be used to compute φ and ρ:

$$\begin{cases} \phi = \arctan\left(\dfrac{a_x}{\sqrt{a_y^2 + a_z^2}}\right), \\ \rho = \arctan\left(\dfrac{a_y}{\sqrt{a_x^2 + a_z^2}}\right). \end{cases} \tag{3.46}$$

These equations guarantee that the accuracy is almost constant inside the whole range of values which φ and ρ can assume, as shown by the dotted and dashed lines in Fig. 3.4.
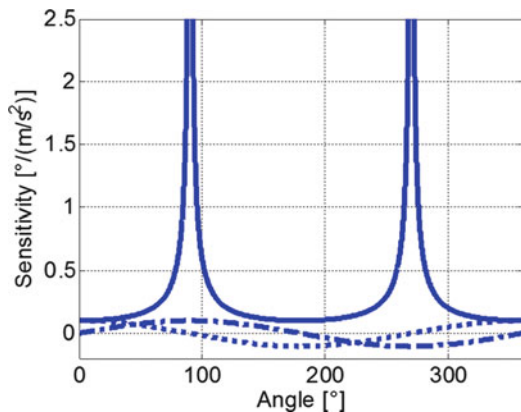
Fig. 3.4 This figure shows the sensitivity of the measured acceleration as a function of the tilt angle. The continuous line refers to (3.45) and it expresses the sensitivity of φ with respect to a_X. The dotted and dashed lines refer to (3.46); the first expresses the sensitivity of φ with respect to a_X and the second one as a function of a_Z. For clarity, these two functions are computed for $a_Y = 0$ (© 2009 IEEE, reprinted with permission)
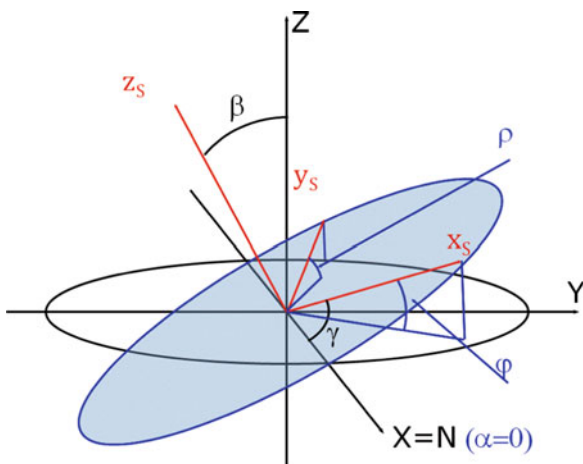

Fig. 3.5 The orientation of the MEMS accelerometer expressed both with the orientation angles ϕ and ρ, and with the Euler angles (α, β, γ). Because the value of α is irrelevant, it is arbitrarily set to 0; consequently, the nodes' axis N coincides with the X axis (© 2009 IEEE, reprinted with permission)

The two angles defined in (3.46) represent two independent orientation parameters in the sense that any error on the estimate on φ does not influence the estimate on ρ and vice versa (Fig. 3.5). Another possible set of angles used to describe orientation is through the Euler's angles. Since these are defined as a sequence of rotations, they do not enjoy the same property of independence, as for the angle set (φ, r).
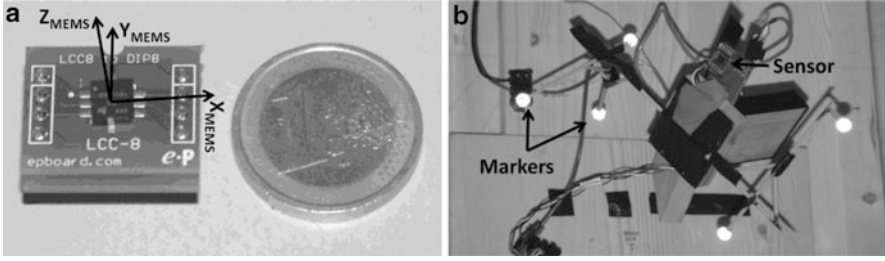
Fig. 3.6 A zoom of the sensor mounted on a board is shown in panel (**a**), along with its local reference system (© 2009 IEEE, reprinted with permission). Panel (**b**) shows the structure on which the sensor was attached with five markers, rigidly connected to the accelerometer (© 2009 IEEE, reprinted with permission)

In order to express the sensor orientation in terms of the Euler angles (α, β, γ), it is possible to derive the relationship between (φ, ρ) and (α, β, γ); this is for instance reported in Appendix A (A3 and A8) of [4]. The following relationships are obtained:

$$
\begin{cases}
\alpha = 0 \text{ (undetermined)}, \\
\sin(\beta) = \sqrt{\sin^2(\phi) + \sin^2(\rho)}, \quad (0 \le \beta \le \pi), \\
\sin(\gamma) = \dfrac{\sin(\phi)}{\sin(\beta)} = \dfrac{\sin(\phi)}{\sqrt{\sin^2(\phi) + \sin^2(\rho)}}.
\end{cases}
\tag{3.47}
$$

Since the angle α expresses a rotation around the absolute vertical axis, it cannot be measured by the accelerometer; it remains undetermined and it can be arbitrary set to zero.

Given these preambles, we can now describe how to evaluate the accuracy of the autocalibration procedure. To this aim, we have compared the orientation angles computed using (3.46), with the same angles provided by a commercial motion capture system, the BTS-SMART3D™ [42]. This system is able to compute the 3D position of a set of retroreflective markers, whose position is surveyed by six cameras. The working volume of the motion capture system was approximately 500 mm × 500 mm × 500 mm, which allowed accommodating different sensor orientations with optimal marker visibility. With this working volume, the markers are localized with an accuracy of 0.1 mm (rms error).

The markers and the accelerometer, rigidly connected to each other, were fixed on a frame that could be oriented in any direction, as shown in Fig. 3.6b. Five markers were located, noncoplanarly, in the vicinity of the accelerometer. The orientation of the supporting structure was then computed as the mean rotational component of the rigid motion undergone by the markers. The angular accuracy in the measurement of this orientation can be derived from the spatial accuracy in the localization of the markers. This can be done by determining the sensitivity of

the angular displacement with respect to a spatial displacement, as described in [45]. For the adopted setup (five markers, spatial accuracy of 0.1 mm (rms), and a minimum distance of 100 mm from the accelerometer) the angular accuracy in the measurement of the orientation of the MEMS results to be better than $0.025°$ (rms).

The vertical direction of the motion capture reference system was carefully established to guarantee that it is parallel to gravity, by surveying two markers, fixed onto the wire of a plumb line, held along the vertical.

Once the vertical direction was determined, and the 3D position of the five markers on the accelerometer board was known for each orientation, the rotation matrix and the corresponding Euler angles (α, β, γ) for each orientation were computed. This has been done by using quaternions [46] that allow determining the rotation by solving a linear system, thereby guaranteeing the orthonormality of the obtained rotation matrix. From the Euler angles, we computed the angles φ_{REF} and ρ_{REF}, which define the reference orientation of the structure, and consequently of the accelerometer, in the motion capture reference system, by exploiting the relationships of (3.47). At the same time, for each sampled orientation, the angles φ_{MEMS} and ρ_{MEMS} were also estimated by processing the MEMS sensor output through (3.46).

The high accuracy of the motion capture system allowed taking its orientation measurements as the ground truth. For this reason, we adopted a comparative approach to evaluate the accuracy of the orientation angles φ and ρ, comparing the value output by the accelerometer to those computed through the motion capture system data.

The estimated orientation angles along with their standard deviation are reported in Table 3.9, which describes the metrological performance of the sensor in the attitude estimation. In particular, we compared the output of the accelerometer before calibration ("Factory" column), calibrated with a six parameter model (excluding therefore the axes misalignments) and with a nine parameters model. The error in the estimated angles ranges from $-23.10°$ to $+6.15°$ when factory calibration data are used. This bias decreases to the range from $-1.54°$ to $+1.15°$, when the six-parameters model is used, and it further decreases to the range from $-0.26°$ to $+0.26°$ when the nine-parameters model is adopted. Such results clearly demonstrate the need for calibrating the sensor and, moreover, the need for including the axes misalignment terms in the sensor model.

To investigate the spatial distribution of the errors we defined the error angles, $\Delta\varphi$ and $\Delta\rho$, as:

$$\begin{cases} \Delta\phi = \phi_{MEMS} - \phi_{REF} \\ \Delta\rho = \rho_{MEMS} - \rho_{REF} \end{cases} \tag{3.48}$$

and plotted them in Fig. 3.7 for one of the sensors (#1). As it can be seen, errors do not show any particular dependence from the sensor orientation: by using factory calibration data (panel (a)) errors are distributed approximately inside a circle centered in [0, 0]. The dimension of this circle is greatly reduced when auto calibration is carried out, and, in particular, when the nine-parameters model is adopted (panel (b)). Panels (c) and (d) show that, thanks to the particular trigonometric formulation of (3.46), the error is isotropic, as it does not depend on

Table 3.9 Mean error and standard deviation of the measured orientation, expressed by angles φ and ρ (first and second section of the table) and with the Euler angles β and γ (third and fourth sections), for the four ST accelerometers calibrated with the factory calibration data (column "Factory"), with the six-parameters model (column "Model 6") and with the nine-parameters model (column "Model 9"). Errors are in degrees

Sensor #	# Samples (N)	Factory	Model 6	Model 9
φ: mean error $\pm$ SD (°)				
#1	72	-2.23 ± 6.84	$+0.24 \pm 0.53$	$+0.18 \pm 0.47$
#2	42	$+3.38 \pm 2.77$	$+0.15 \pm 0.60$	-0.21 ± 0.59
#3	35	-23.10 ± 3.37	-1.54 ± 1.81	-0.26 ± 1.44
#4	35	-14.90 ± 4.86	$+0.58 \pm 0.91$	-0.20 ± 0.74
ρ: mean error $\pm$ SD (°)				
#1	72	-0.05 ± 6.40	-0.09 ± 0.65	$+0.11 \pm 0.59$
#2	42	$+0.80 \pm 2.52$	$+0.41 \pm 0.51$	$+0.03 \pm 0.34$
#3	35	$+0.77 \pm 10.38$	$+1.15 \pm 1.66$	$+0.26 \pm 1.11$
#4	35	$+6.15 \pm 8.12$	-0.42 ± 0.68	$+0.00 \pm 0.50$
β: mean error $\pm$ SD (°)				
#1	72	$+1.47 \pm 11.17$	-0.01 ± 0.59	$+0.11 \pm 0.59$
#2	42	-0.34 ± 3.18	-0.09 ± 0.56	$+0.03 \pm 0.56$
#3	35	-8.34 ± 10.73	-0.57 ± 1.34	-0.31 ± 1.11
#4	35	-8.62 ± 12.60	$+0.31 \pm 0.56$	-0.03 ± 0.47
γ: mean error $\pm$ SD (°)				
#1	72	-1.99 ± 4.37	$+0.31 \pm 1.02$	$+0.23 \pm 0.81$
#2	42	$+5.28 \pm 7.22$	$+0.24 \pm 0.61$	-0.10 ± 0.37
#3	35	-27.11 ± 13.38	-0.94 ± 6.48	-0.46 ± 1.76
#4	35	-18.81 ± 22.34	$+0.99 \pm 1.81$	-0.12 ± 0.45

the values assumed by φ and ρ. Similar results are obtained for the other calibrated accelerometers.

The results reported in the column "Model 6" of Table 3.9 show a residual error of the order of few degrees on the orientation measurements, while measurement error was as large as 20° with factory calibration data (sensor #3). However, accuracy can be further improved considering also the misalignment term in the sensitivity matrix, leading to the nine-parameters model (column "Model 9"). With this model, the accuracy was reduced to less than one degree ($\pm 0.26°$). The improvement with respect to the six-parameters model is therefore almost of one order of magnitude and consistent in all the calibration experiments. This fact, together with the very low uncertainty in the parameter estimate (see Tables 3.6, 3.7 and 3.8), can be reasonably interpreted as a better model-fitting capability of the nine-parameters model, with respect to the six-parameters model. This allows drawing the conclusion that the axes misalignment parameters in the model allow a better fitting of the physical sensor behavior.

The value of sensitivities and biases obtained through auto calibration is generally close but not equal to that provided by the manufacturer; typical differences are in the order of ± 10 % for the bias and ± 5 % for the scale factor (cf. Tables 3.6, 3.7 and 3.8).
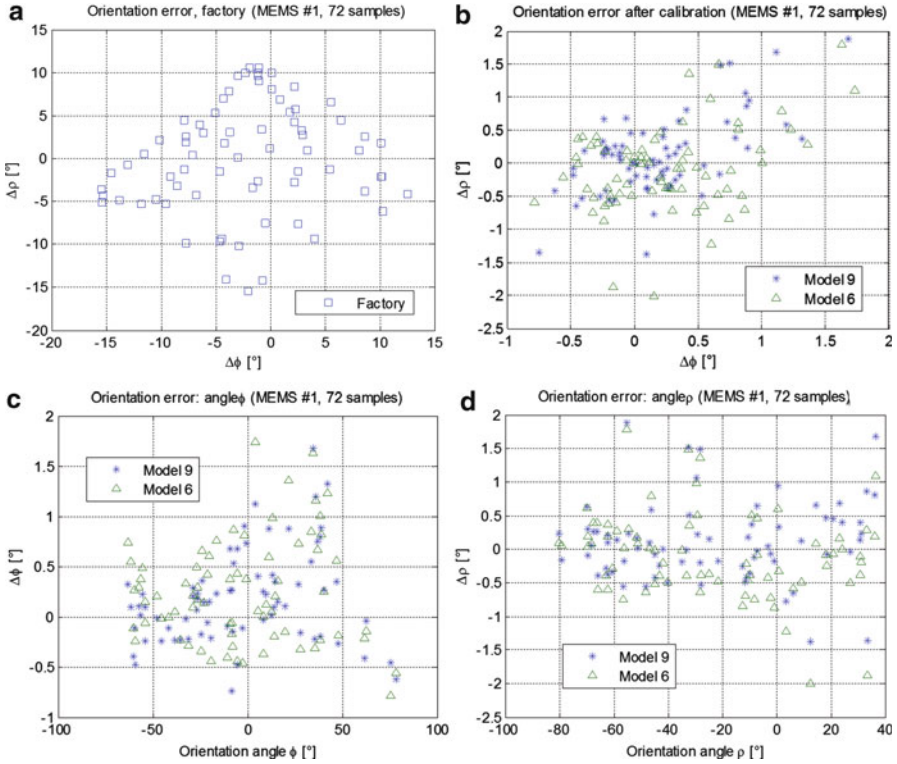
Fig. 3.7 Error in the estimate of φ and ρ, for the 72 orientations measured for sensor #1 (© 2009 IEEE, reprinted with permission)

However, when they are used to compute the sensor orientation, this error is amplified: the error was in some cases larger than 20° (sensor #3 in Table 3.9), with standard deviation exceeding 10°, when the values of **S** and **o** given by the factory (and null axes misalignment) were used. Nevertheless, factory parameters can be used as a reliable initialization point for Newton's optimization and a small number of iterations are sufficient to obtain a reliable and accurate estimate of the sensor parameters.

3.6.3 From the Sensitivity Matrix to the Axes Misalignments

From the inverse sensitivity matrix $\mathbf{S}^{-1}$ computed in calibration, the matrix **S** is easily obtained and the axes misalignments can be computed from the decomposition of **S** into a rotation matrix and a lower triangular matrix [see (3.9)–(3.11)]. This also allows computing the sensitivity of each sensor channel. An example of such decomposition is illustrated at the beginning of the chapter. The estimated angles between the axes of the accelerometers considered here are reported in Table 3.10. For the LIS3L02AL accelerometer, deviations from the orthogonality as large as 3° have been measured.

Table 3.10 Estimated angles between the sensing axes of the sensor

	XY (°)	XZ (°)	YZ (°)
LIS3L02AL (ST) #1	89.108	90.518	90.059
LIS3L02AL (ST) #2	88.778	89.593	90.155
LIS3L02AL (ST) #3	92.737	92.926	90.943
LIS3L02AL (ST) #4	88.681	89.225	89.453
ADXL330 (AD—Wii)	88.387	90.035	90.080

The nominal value is 90° for both the LISL02AL and ADXL330 sensors

3.6.4 Calibration of Another Sensor: ADXL330 (Wiimote Accelerometer)

In this paragraph, we report the calibration results obtained for the ADXL333 triaxial accelerometer by Analog Device, which is included in the Wiimote controller. The accelerometer was calibrated from the data measured on a sequence of $N = 49$ random sensor orientations. For each orientation, the sensor was maintained still for a certain amount of time and an average number of 165 measured accelerations were acquired for each orientation; these were then averaged to build the input of the autocalibration procedure. Thanks to the noise independency among different samples, the noise on the measured acceleration can be reduced through averaging, and therefore the accuracy of the estimated parameters increases. In particular, averaging 165 samples each corrupted by a Gaussian noise with zero mean and variance σ^2, produce a Gaussian random variable with variance reduced to $\sigma^2/165$. For the sensor considered here, this is indispensable to get a reliable estimate of the axes misalignments. Results of the calibration (estimated values together with their estimated standard deviations) are reported in Tables 3.6, 3.7 and 3.8, whereas in Table 3.10 the estimated angles between the sensor axes are reported.

Notice that the misalignments of the axes of the ADXL330 sensor results to be smaller than that of the LIS3L02AL sensor. This is coherent with what reported in the sensor datasheets [27, 28]: a 2 % cross-axis term is expected for the LIS3L02AL sensor, whereas a 1 % cross-axis term is declared for the ADXL330 accelerometer. Notice, however, that the second sensor is noisier than the first one; as a consequence, the uncertainty of the off-diagonal terms in $\mathbf{S}^{-1}$ is comparable with the estimated values for these terms (see Table 3.8—for instance, the standard deviation of s^{-1}_{XZ} is 72 % of its estimated value). This fact suggests that, when a noisy sensor is used, the six parameter model could provide a more accurate estimate of the sensor parameters. In fact, the nine-parameters model can be used even in this case, but the estimate of the cross-axis term would be unreliable. Notice, at last, that without averaging the 165 measured accelerations, the standard deviations reported in Table 3.9 should be about 12 times larger; this would make the estimate of the axes misalignments completely unreliable.

3.7 Conclusion

We summarize here the main aspects involved in the autocalibration of MEMS accelerometers, described in this chapter. Each of this has to be carefully considered before designing a proper autocalibration procedure, taking into account the specific application and the sensor characteristics.

3.7.1 Choice of the Sensor Model

The choice of the most adequate sensor model depends on two main factors: the specific application in which the sensor is involved, and the noise characteristics of the sensor. The simplest model include only one sensitivity and one offset parameters, and it is suited for applications like [9], where the accelerometer is used to roughly detect the posture of a human being; because of the low number of parameters, this model can be adopted also for very noisy sensors. On the opposite, the most refined sensor models may include nonlinearities, hysteresis [16] or even the electrical cross talk between the channels [4]. The analysis of the literature, however, highlights that models with more than nine parameters often lead to an unreliable estimate of the parameters, and therefore do not contribute to increase the overall accuracy of the sensor. As a general rule, we can state that the nine parameter model, including three offsets and sensitivities and the axes misalignments, is generally suited for most applications and produces an accurate estimate of the model parameters. In case of noisy sensor, like the ADXL330 by Analog Device considered here, even this model can be over-parameterized; in this case, a proper noise reduction strategy has to be adopted; otherwise, a simpler six parameters model has to be used.

3.7.2 Modeling the Sensor Noise

Many authors assume the noise on the measured acceleration vector to be distributed as a zero mean, Gaussian vector. This is actually true, as shown in (3.15). However, we have also clearly demonstrated that, starting from the hypothesis of Gaussian vector on the measured sensor output, the squared norm of the measured acceleration vector is affected by a zero mean Gaussian component plus a χ^2 component, whose mean differs from zero and it is proportional to the variance of the sensor noise. In many practical cases, the bias introduced he by this component is little when compared with the static gravity acceleration (see Table 3.1) and it can be neglected during the calibration procedure. However, when small accelerations have to be measured, as for instance illustrated by the example in Fig. 3.2, neglecting this term can strongly bias the computation performed from the measured accelerations (see Table 3.2).

3.7.3 The Right Value of g

All the autocalibration procedures are based on the assumption that, in static conditions, the norm of the measured acceleration vector equals the value of the gravity acceleration, g. However, only a few authors explicitly consider that the value of g strongly depends by the latitude, altitude and other factors. Latitude and altitude, in particular, are responsible for the major changes in the values of g, which can go beyond 0.5 % of its nominal values. Equation (3.24) provides an accurate estimate of g as a function of these parameters. Other phenomena, like tidal or gravity anomalies, are responsible of minor changes in the value of g, and can generally be neglected.

Correcting the value of g before calibration is actually not necessary when the accelerometer is used as a pure tilt sensor; in fact, in this case the only useful information is represented by the orientation of the measured acceleration vector; however, when the sensor is used in quasi static condition in a IMU, the norm of the acceleration vector is taken in consideration: in this case, correcting the value of g is absolutely necessary; otherwise, drifts of hundred of meters can be accumulated in less than 1 min.

3.7.4 Accuracy of the Estimated Parameters

The covariance analysis illustrated in the chapter represents an easy-to-use and powerful tool to determine the effectiveness of the calibration procedure. More generally, such analysis permits to determine whether some parameters of the adopted model cannot be reliably estimated; based on this information, one can decide to reduce the parameters of the sensor model, or to increase the size of the dataset used for calibration. Overall, the covariance analysis should always be performed after calibration to identify possibly critical situations.

3.7.5 Axes Misalignments from Calibration Data

From the calibration data, and in particular from the decomposition of the sensitivity matrix into a rotation and a lower triangular matrix, it is possible to derive the angles between the sensing axes of the accelerometer. This information can be useful for the producer, that has to control the consistency of the produced sensors; it can also be used to verify that the calibration has produced reasonable values of the sensor parameters; at last, it can be used to verify the correct alignment of monoaxial and biaxial accelerometers, that are often manually composed to construct a triaxial sensor.

References

1. Rudolf F, Frosio R, Zwahlen P, Dutoit B (2009) Accelerometer with offset compensation. US Patent 2009/0223276 A1, 10 September 2009
2. Olney A (2010) Evolving MEMS qualification requirements. In: Proceedings of IEEE international reliability physics symposium (IRPS), pp 224–230, Wilmington, MA, USA, May 2010
3. Tadigadapa S, Mateti K (2009) Piezoelectric MEMS sensors: state-of-the-art and perspectives. Meas Sci Technol 20:092001 (30 pp)
4. Frosio I, Pedersini F, Stuani S, Borghese NA (2009) Autocalibration of MEMS accelerometers. IEEE Trans Instrum Meas 58(6):2034–2041
5. Łuczak S, Oleksiuk W, Bodnicki M (2006) Sensing tilt with MEMS accelerometers. IEEE Sensor J 6(6):1669–1675
6. Giansanti D, Maccioni G, Macellari V (2005) The development and test of a device for the reconstruction of 3-D position and orientation by means of a kinematic sensor assembly with rate gyroscopes and accelerometers. IEEE Trans Biomed Eng 52(7):1271–1277
7. Pérez R, Costa Ú, Torrent M, Solana J, Opisso E, Cáceres C, Tormos JM, Medina J, Gómez EJ (2010) Upper limb portable motion analysis system based on inertial technology for neurorehabilitation purposes. Sensors 10(12):10733–10751
8. Roetenberg D, Slycke PJ, Veltink PH (2007) Ambulatory position and orientation tracking fusing magnetic and inertial sensing. IEEE Trans Biomed Eng 54(5):883–890
9. Curone D, Bertolotti GM, Cristiani A, Secco EL, Magenes G (2010) A real-time and self-calibrating algorithm based on triaxial accelerometer signals for the detection of human posture and activity. IEEE Trans Inf Technol Biomed 14(4):1098–1105
10. Utters JC, Schipper J, Veltink PH, Olthuis W, Bergveld P (1998) Procedure for in-use calibration of triaxial accelerometers in medical applications. Sensor Actuator A68:221–228
11. Camps F, Harasse S, Monin A (2009) Numerical calibration for 3-axis accelerometers and magnetometers. In: Proceedings of the IEEE international conference on electro/information technology, pp 217–221, Toulouse, France, June 2009
12. Tan CW, Park S (2005) Design of accelerometer-based inertial navigation systems. IEEE Trans Instrum Meas 54(6):2520–2530
13. Syed ZF, Aggarwal P, Goodall C, Niu X, El-Sheimy N (2007) A new multi-position calibration method for MEMS inertial navigation systems. Meas Sci Technol 18:1897–1907
14. Aggarwal P, Syed Z, Niu X, El-Sheimy N (2006) Cost-effective testing and calibration of low cost MEMS sensors for integrated positioning, navigation and mapping systems. In: Shaping the change XXIII FIG Congress Munich, Germany, 8–13 October 2006
15. Wang J, Liu Y, Fan W (2006) Design and calibration for a smart inertial measurement unit for autonomous helicopters using MEMS sensors. In: Proceedings of the 2006 I.E. international conference on mechatronics and automation, Luoyang, China, 25–28 June 2006
16. Lang P, Pinz A (2005) Calibration of hybrid vision/inertial tracking systems. In: Proceedings of the second InerVis: workshop on integration of vision and inertial senors, Barcelona, Spain, 18 April 2005
17. Dong Z, Zhang G, Luo Y, Tsang CC, Shi G, Kwok SY, Li WJ, Leong PHW, Wong MY (2007) A calibration method for MEMS inertial sensors based on optical tracking. In: Proceedings of the second IEEE international conference on nano/micro engineered and molecular systems, Bangkok, Thailand, 16–19 January 2007
18. Dong Z, Uchechukwu C, Wejinya C, Zhou S, Shan Q, Li WJ (2009) Real-time written-character recognition using MEMS motion sensors: calibration and experimental results. In: Proceedings of the 2008 I.E. international conference on robotics and biomimetics, Bangkok, Thailand, 21–26 February 2009.
19. Freedson P, Pober D, Janz KF (2005) Calibration of accelerometer output for children. Med Sci Sports Exerc 37(11 Suppl):S523–S530
20. King K, Yoon SW, Perkins NC, Najafi K (2008) Wireless MEMS inertial sensor system for golf swing dynamics. Sensor Actuator A 141:619–630

21. Zhao M, Xiong X (2009) A new MEMS accelerometer applied in civil engineering and its calibration test. In: The ninth international conference on electronic measurement & instruments ICEMI'2009, Shanghai, China, 2:122–125, Aug. 2009
22. Ratcliffe C, Heider D, Crane R, Krauthauser C, Keun Yoon M, Gillespie JW Jr (2008) Investigation into the use of low cost MEMS accelerometers for vibration based damage detection. Compos Struct 82:61–70
23. Zanjani PN, Abraham A (2010) A method for calibrating micro electro mechanical systems accelerometer for use as a tilt and seismograph sensor. In: 2010 12th international conference on computer modelling and simulation, pp 637–641, Theran, Iran, March 2010
24. Krohn A, Beigl M, Decker C, Kochendorfer U, Robinson P, Zimmer T (2005) Inexpensive and automatic calibration for acceleration sensors. In: Ubiquitous computing systems, Lecture notes in computer science, vol 3598/2005, pp 245–258, DOI: 10.1007/11526858_19
25. Pylvanainen T (2008) Automatic and adaptive calibration of 3D field sensors. Appl Math Model 32:575–587
26. Golub GH, Van Loan CF (1996) Matrix computations, 3rd edn. Johns Hopkins, Baltimore. ISBN 978-0-8018-5414-9
27. STMicroelectronics (2004) LIS3L02AL 3axis-2g linear accelerometer [Online]. http://www.st.com/stonline/
28. Analog Devices (2006) ADXL330 3-axis-3g linear accelerometer [Online]. http://www.analog.com/static/imported-files/data_sheets/ADXL330.pdf
29. Nintendo Wii console web-site [Online]. http://www.nintendo.com/wii
30. Shen SC, Chen CJ, Huang HJ (2010) A new calibration method for MEMS inertial sensor module. In: The 11th IEEE international workshop on advanced motion control, Nagaoka, Japan, 21–24 March 2010
31. Ketelhohn CH (2004) Accelerometer-based infant movement monitoring and alarm device. US Patent 6765489, 20 July 2004
32. Kolen PT (2008) Infant SID monitor based on accelerometer. Publication No. US 2008/0262381 A1, 23 October 2008
33. Luczak S, Oleksiuk W (2007) Increasing the accuracy of tilt measurements. Eng Mech 14(1):143–154
34. Ang WT, Khosla PK, Riviere CN (2007) Nonlinear regression model of a low-g MEMS accelerometer. IEEE Sensor J 7(1):81–87
35. Boynton R (2001) Precise measurement of mass. In: 60th annual conference of the society of allied weight engineers, SAWE Paper no. 3147, Arlington, TX, 21–23 May 2001
36. NASA GRACE mission homepage [Online]. http://www.csr.utexas.edu/grace/
37. Ramprasad T (2007) The earth's gravitational field, refresher course on marine geology and geophysics [Online]. Lecture Notes, pp 191–195. http://drs.nio.org/drs/handle/2264/720
38. Wu ZC, Wang ZF, Ge Y (2002) Gravity based online calibration for monolithic triaxial accelerometers' gain and offset drift. In: Proceedings of the 4th world congress intelligent control and automation, pp 2171–2175, Shanghai, China, June 2002
39. Madsen K, Nielsen HB, Tingleff O (2004) Methods for non-linear least squares problems, 2nd edn. IMM Technical University, Lyngby, Denmark
40. Dumas N, Azaïs F, Mailly F, Nouet P (2009) A method for electrical calibration of MEMS accelerometers through multivariate regression. In: Mixed-signals, sensors, and systems test workshop, 2009. IMS3TW '09. IEEE 15th International, 10–12 June 2009, pp 1–6
41. Dumas N, Azaïs F, Mailly F, Nouet P (2008) Evaluation of a fully electrical test and calibration method for MEMS capacitive accelerometers. In: Proceedings on IEEE mixed-signals, sensors, and systems test workshop, pp 1–6, Vancouver, BC, Canada, June 2008
42. BTS website [Online]. http://www.bts.it
43. Winter D (1990) Biomechanics and motor control of human movement. Wiley, New York
44. Press WH, Teukolsky SA, Vetterling WT, Flannery BP (2003) Numerical recipes: the art of scientific computing, 3rd edn. Cambridge University Press, New York
45. Barford NC (1985) Experimental measurements: precision, error and truth. Wiley, Hoboken, NJ
46. Alonso M, Finn EJ (1974) Fundamental university physics. Fields and waves, vol 2. Inter European Editions, Amsterdam